# Measurement of Tidal Form Drag Using Seafloor Pressure Sensors

SALLY J. WARNER AND PARKER MACCREADY

*School of Oceanography, University of Washington, Seattle, Washington*

JAMES N. MOUM AND JONATHAN D. NASH

*College of Earth, Ocean, and Atmospheric Sciences, Oregon State University, Corvallis, Oregon*

ABSTRACT

As currents flow over rough topography, the pressure difference between the up- and downstream sides results in form drag—a force that opposes the flow. Measuring form drag is valuable because it can be used to estimate the loss of energy from currents as they interact with topography. An array of bottom pressure sensors was used to measure the tidal form drag on a sloping ridge in 200 m of water that forms a 1-km headland at the surface in Puget Sound, Washington. The form drag per unit length of the ridge reached $1 \times 10^4$ N m$^{-1}$ during peak flood tides. The tidally averaged power removed from the tidal currents by form drag was 0.2 W m$^{-2}$, which is 30 times larger than power losses to friction. Form drag is best parameterized by a linear wave drag law as opposed to a bluff body drag law because the flow is stratified and both internal waves and eddies are generated on the sloping topography. Maximum turbulent kinetic energy dissipation rates of $5 \times 10^{-5}$ W kg$^{-1}$ were measured with a microstructure profiler and are estimated to account for 25%–50% of energy lost from the tides. This study is among the first to measure form drag directly using bottom pressure sensors. The measurement and analysis techniques presented here are suitable for periodically reversing flows because they require the removal of a time-mean signal. The advantage of this technique is that it delivers a continuous record of form drag and is much less ship intensive compared to previous methods for estimation of the bottom pressure field.

## 1. Introduction

In the ocean, form drag occurs when currents flow over rough topography creating a pressure difference between the upstream and downstream sides of an object within a flow field. Form drag differs from frictional drag, which is due to shear stresses acting within the bottom boundary layer. Often form drag has a magnitude that is much larger than frictional drag (Nash and Moum 2001), however, form drag is patchy because it only occurs in regions of rough topography. Unlike frictional drag, which acts only in the bottom boundary layer, form drag leads to mixing and turbulence throughout the water column and creates eddies and internal waves that carry energy away from the topography (Polzin et al. 1997; Jayne and St. Laurent 2001; Rudnick et al. 2003; Pawlak et al. 2003; Garrett and Kunze 2007).

The magnitude of frictional drag is relatively well parameterized, whereas form drag parameterizations are difficult to formulate since much less is known about the magnitude and spatial distribution of form drag despite some recent advances (Nikurashin and Ferrari 2011).

An eventual goal of form drag research is to improve drag parameterizations in large-scale numerical models. Models often neglect form drag because they do not resolve the scales at which form drag occurs, which can lead to overprediction of velocities (Oke et al. 2002). Better drag parameterizations will likely improve ocean model current predictions as they have for atmospheric weather prediction models (Lott and Miller 1997; Wood et al. 2001; Kim et al. 2003). Additionally, the inclusion of form drag parameterizations into large-scale models may be helpful in constraining the distribution of turbulent mixing in the ocean interior, since form drag creates power available for mixing away from the boundaries themselves.

Total form drag—due to bottom pressure anomalies—has not previously been measured in the ocean. Only the parts related to changes in isopycnal height (referred to
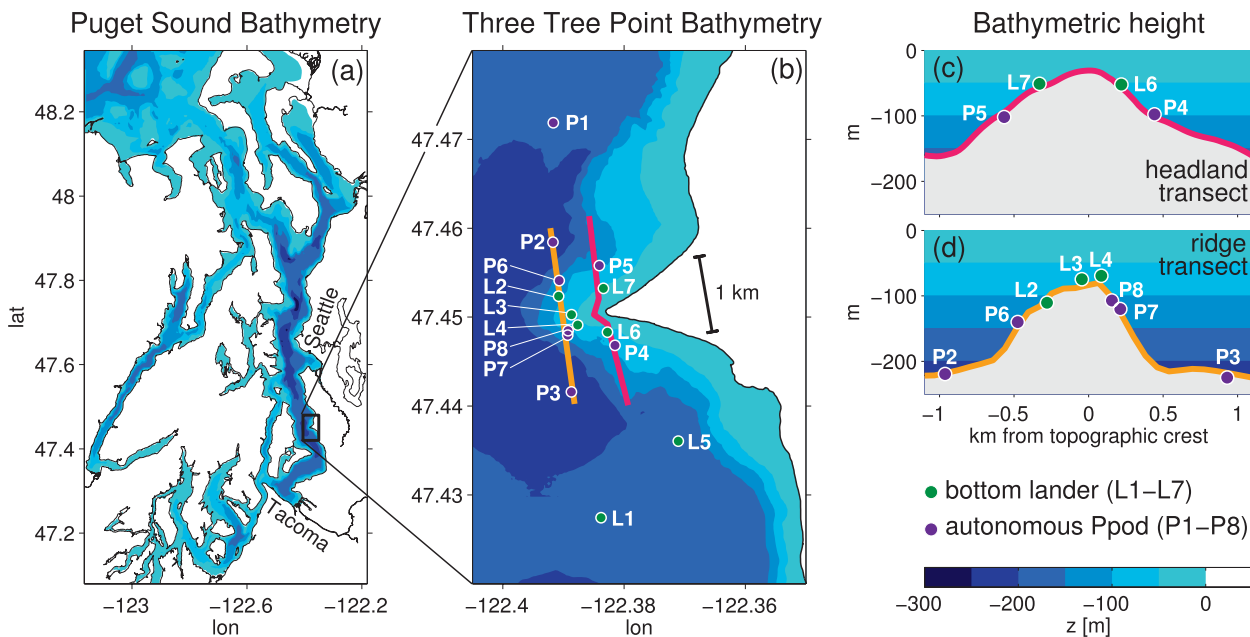
FIG. 1. (a) Puget Sound bathymetry. TTP is located between Seattle and Tacoma in a relatively straight section of the Main Basin. (b) TTP bathymetry. The location of the two ship transects (yellow and magenta lines), bottom landers (green markers), and autonomous Ppods (purple markers) are shown. (c) The bathymetric height and instrument locations along the headland transect. The transect is oriented as if the viewer is looking from the center of the channel toward land with north to the left and south to the right. In this orientation, flood tides flow from left to right. (d) The bathymetric height and instrument locations along the ridge transect.

in this paper as internal form drag) (Moum and Nash 2000; Nash and Moum 2001; Edwards et al. 2004) and perturbations of the sea surface (here called external form drag) (McCabe et al. 2006) have been quantified. In this experiment, total form drag was measured with pressure sensors in a similar way to mountain drag in the atmosphere (Bougeault et al. 1993). Precise bottom pressure sensors (Ppods) (Stöber and Moum 2011) were deployed across the bathymetry near Three Tree Point (TTP), a headland in Puget Sound, Washington, with predictable tidal currents. TTP has been studied extensively in the past: Edwards et al. (2004) and McCabe et al. (2006) quantified the internal and external form drag, respectively, Canals et al. (2009) described the tilted eddies present there, and Warner and MacCready (2009, hereafter WM09) showed with a numerical model that there is an additional part of the form drag that arises in oscillatory flow situations ("inertial" form drag). In this study, total form drag from bottom pressure sensors, "bulk" drag estimated from the shallow water momentum equation, internal form drag, inertial form drag (arising from tidal time-dependence), frictional drag, and turbulent dissipation are all quantified.

There are three goals of this paper: first, to present a new method for measuring form drag on undersea topography using bottom pressure gauges; second, to parameterize form drag in terms of existing drag laws; and

finally, to determine what physical mechanisms create form drag at TTP. Field observations are described in section 2. Bottom pressure measurements are discussed in section 3. In section 4, form drag is calculated from bottom pressure anomalies. The density, microstructure, and velocity measurements and their implications for form drag are described in sections 5, 6, and 7. The inertial drag is discussed in section 8. Finally, the results of this study are compared to form drag parameterizations in section 9. A set of conclusions follows in section 10.

## 2. Experiment details

TTP is a triangular headland located in a relatively straight section of the Main Basin of Puget Sound (Fig. 1). At the surface, it is ~1 km wide in the along-channel direction and it extends as a sloping ridge 1.5 km into the 5-km-wide channel. The mean depth in this region is 200 m. TTP has very steep sidewalls with a mean slope of 1:5, which is supercritical relative to internal waves at the $M_2$ frequency.

The field experiment took place from 25 October through 1 November 2010. Eight autonomous Ppods (P1-P8) were deployed along two transect lines (Figs. 1b–d). They are modified Paroscientific pressure sensors, which have a precision of 1.4 Pa and take measurements every second (Moum and Nash 2008). In addition, seven bottom
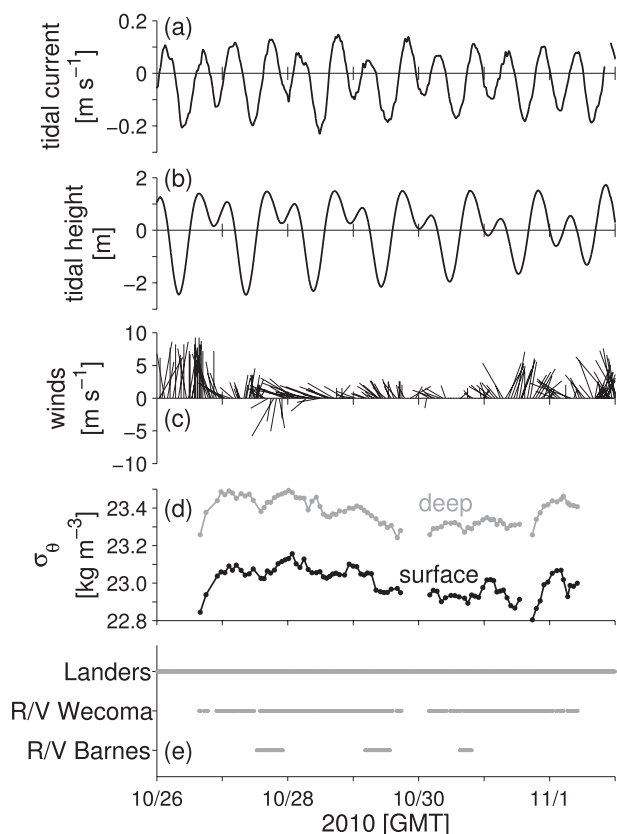
FIG. 2. (a) Tidal currents ($u_0$). Floods tides are negative because they flow to the south. (b) Tidal height [$\overline{\eta} = 0.5(p_{L1} + p_{P1})/(\rho_0 g)$]. (c) Wind speed and direction. The wind was blowing from the south throughout the majority of the experiment. (d) Potential density for surface waters (less than 20 m) and deep waters (greater than 20 m). (e) Periods of instrument deployment and ship transects.

landers (L1-L7), each equipped with an upward look-ing RDI ADCP (150, 300, or 1200 kHz, depending on depth), a SBE Microcat, a Ppod, and an acoustic release were deployed. For stability, the landers had to be placed on relatively flat areas, therefore L3 and L4 were positioned slightly off the transect lines. L5 was placed on the south side of the topography to observe the lee eddies during flood tides. Both the ADCP and the Ppod on lander 7 failed, and were not used in the analysis.

Two ships took measurements along the transects (Figs. 1b and 2e). Along the ridge transect, the R/V *Wecoma* collected continuous ship-mounted ADCP and echosounder data. A Chameleon profiler (Moum et al. 1995) was yo-yoed from the stern measuring salinity, temperature and microstructure. Chameleon was drop-ped until it hit the bottom or to 160 m, whichever was shallower, allowing at least 10 casts per transect. Be-tween 26 October and 1 November, 90 transects were completed each taking about an hour to go southward while taking Chameleon measurements and a half hour

to return back to the start. Along the headland transect, the R/V *Barnes* collected ship-mounted ADCP veloci-ties for 10 h on 27 October, for 9 h on 29 October, and for 5 h on 30 October. The schedule was chosen to capture the flow patterns during strong flood and ebb tides. There were four CTD stations along the headland transect that were performed with a SBE 19 SEACAT Profiler.

In Puget Sound, tides are mixed semidiurnal with flood tides flowing to the south (Figs. 2a,b). Flood currents are faster than ebb currents at TTP because of topographic siphoning of the ebb currents through Colvos Passage rather than through the channel where TTP is located (Bretschneider et al. 1985). The experiment took place during neap tide; therefore, it is likely that our estimates for form drag are lower than they would be during spring tides. The background tidal velocity ($u_0$, Fig. 2a) was found by vertically averaging the ADCP velocity from the L1 lander. The top and bottom 30 m are ignored to avoid effects of wind and bottom boundary layer pro-cesses. Principle component analysis (Emery and Thomson 2004) was used to find the dominant current direction, which aligns closely to the along-channel di-rection. It was then low-pass filtered with a 60-min Hanning window to get a smooth tidal velocity signal. The winds were from the south and always less than 10 m s$^{-1}$ (Fig. 2c). They were especially weak during the time of the ship transecting. The potential density changed slightly throughout the experiment, but the stratification remained relatively constant (Fig. 2d).

## 3. Bottom pressure anomalies

### a. Calculating bottom pressure anomalies from Ppods

Form drag ($D_{\text{form}}$) is defined as the spatial integral of the bottom pressure times the bottom slope. A detailed derivation of the along-channel component of form drag from the momentum equation can be found in McCabe et al. (2006),

$$D_{\text{form}}(t) = -\int_{x_1}^{x_2} p'_{\text{bot}}(x, y, t) h_x \, dx, \qquad (1)$$

where $p'_{\text{bot}}$ is the bottom pressure anomaly, $h$ is the bottom height, $h_x$ is the bottom slope in the along-channel direction, and $x_1$ and $x_2$ are points of equal depth on either side of the topography. As defined here, $D_{\text{form}}$ has units of Newtons per meter cross-channel distance. The sign of (1) indicates that form drag re-moves momentum from the flow. The associated power ($P_{\text{form}}$), or rate of energy loss from the mean flow, is the

product of the form drag and the background tidal velocity, $u_0$ (Gill 1982, section 8.7):

$$P_{\text{form}} = D_{\text{form}} u_0. \qquad (2)$$

This definition of power is chosen because it encompasses energy losses both from internal waves and from eddies. The form drag power, $P_{\text{form}}$, should not be confused with barotropic to baroclinic energy conversion (Kelly et al. 2010), which is appropriate for topography that only generates internal waves, but does not work in regions of the topography dominated by eddies.

Ppods measure the total pressure at the seafloor ($p_{\text{bot}}$). The total pressure is dominated by the resting depth and spatially averaged tidal height variations, which do not contribute to form drag. To find the bottom pressure anomaly ($p'_{\text{bot}}$), we follow Moum and Smyth (2006) and start with the vertical momentum equation for a nonrotating, inviscid, Boussinesq fluid:

$$\frac{\partial p}{\partial z} = -\rho g - \rho_0 \frac{Dw}{Dt}, \qquad (3)$$

where $p = p(\mathbf{x}, t)$ is the total pressure that varies in all directions [$\mathbf{x} = (x, y, z)$] and in time ($t$), $z$ is positive up, $\rho = \rho(\mathbf{x}, t)$ is the density, $\rho_0 = 1023$ kg m$^{-3}$ is a constant background density, and $g$ is gravity. The material derivative is defined as

$$\frac{D}{Dt} \equiv \frac{\partial}{\partial t} + u\frac{\partial}{\partial x} + v\frac{\partial}{\partial y} + w\frac{\partial}{\partial z},$$

where ($u$, $v$, $w$) are the velocities in the along-channel, across-channel, and vertical directions. The density can be broken into three parts, $\rho(\mathbf{x}, t) = \rho_0 + \overline{\rho}(z, t) + \rho'(\mathbf{x}, t)$, where $\overline{\rho}(z, t)$ is the background stratification, and $\rho'(\mathbf{x}, t)$ is the remaining density perturbation. Substituting into (3) and integrating vertically, we obtain

$$p(\mathbf{x}, t) = g\rho_0[\eta(x, y, t) - z] + g\int_z^\eta \overline{\rho}(z, t)\, dz$$
$$+ g\int_z^\eta \rho'(\mathbf{x}, t)\, dz + \rho_0 \int_z^\eta \frac{Dw}{Dt}\, dz. \qquad (4)$$

Next, we divide the sea surface height into three parts: $\eta(x, y, t) = \overline{\eta}(t) + \eta_{\text{tilt}}(x, t) + \eta'(x, y, t)$. Here, $\overline{\eta}(t)$ is a spatial average of the sea surface, $\eta_{\text{tilt}}(x, t)$ accounts for an along-channel tilt of the sea surface due to tidal acceleration, and $\eta'(x, y, t)$ is the remaining sea surface anomaly. We include $\eta_{\text{tilt}}$ as a separate term because it contributes to form drag differently than $\overline{\eta}$ or $\eta'$. Substitute into (4) to obtain an expression for the total pressure:

$$p(\mathbf{x}, t) = \rho_0 g\overline{\eta}(t) + \underbrace{\rho_0 g\eta_{\text{tilt}}(x, t)}_{\star} + \underbrace{\rho_0 g\eta'(x, y, t)}_{\star} - \rho_0 gz$$
$$+ g\int_z^\eta \overline{\rho}(z, t)\, dz + \underbrace{g\int_z^\eta \rho'(\mathbf{x}, t)\, dz}_{\star} + \underbrace{p_{\text{nh}}(\mathbf{x}, t)}_{\star}. \qquad (5)$$

Only the starred terms in (5) vary in $x$ and thus contribute to form drag. The first term, $\rho_0 g\overline{\eta}(t)$, is due to the up and down motion of the tides and is the same everywhere within the domain. The second term, $\rho_0 g\eta_{\text{tilt}}(x, t)$, is used to calculate the inertial form drag (WM09), which is the part owing to the oscillatory nature of the tides and is discussed in detail in section 8. The third term, $\rho_0 g\eta'(x, y, t)$, accounts for local perturbations of the sea surface and $\eta'$ can have a magnitude of a few centimeters at the center of eddies (McCabe et al. 2006). The fourth term, $-\rho_0 gz$, accounts for the depth of each pressure sensor. The fifth term, $g\int_z^\eta \overline{\rho}(z, t)\, dz$, is the pressure owing to a spatially averaged stratification and does not vary horizontally within the domain. The sixth term, $g\int_z^\eta \rho'(\mathbf{x}, t)\, dz$, accounts for vertical displacement of isopycnals, most obviously created by internal lee waves and eddies. Finally, the nonhydrostatic pressure, $p_{\text{nh}}(\mathbf{x}, t)$, cannot be resolved because we do not measure vertical accelerations at every Ppod location. We assume that it will not be a significant part of the signal because Moum and Smyth (2006) show that the nonhydrostatic pressure is much smaller than the hydrostatic pressure for nonlinear internal waves on the continental slope. If nonhydrostatic pressure is present, it will be measured by the Ppods but not differentiated as a separate term. The pressure anomaly that is dynamically relevant to form drag includes the starred terms from (5):

$$p'(\mathbf{x}, t) = \underbrace{\rho_0 g\eta_{\text{tilt}}(x, t)}_{p'_{\text{inert}}} + \underbrace{\rho_0 g\eta'(x, y, t)}_{p'_{\text{ext}}}$$
$$+ \underbrace{g\int_z^\eta \rho'(\mathbf{x}, t)\, dz}_{p'_{\text{int}}} + p'_{\text{nh}}(\mathbf{x}, t), \qquad (6)$$

where $p'_{\text{inert}}$, $p'_{\text{ext}}$, and $p'_{\text{int}}$ are the inertial, external, and internal pressure anomalies, respectively. The pressure anomaly $p'$ can be evaluated at the sea floor to get the bottom pressure anomaly $p'_{\text{bot}}$, which is used to calculate form drag with (1). Form drag can also be calculated with each part of $p'_{\text{bot}}$. For instance, internal form drag ($D_{\text{int}}$) is calculated with $p'_{\text{int}}$.

This pressure decomposition is most appropriate for topography that generates both internal waves and eddies. It differs from other pressure decompositions.
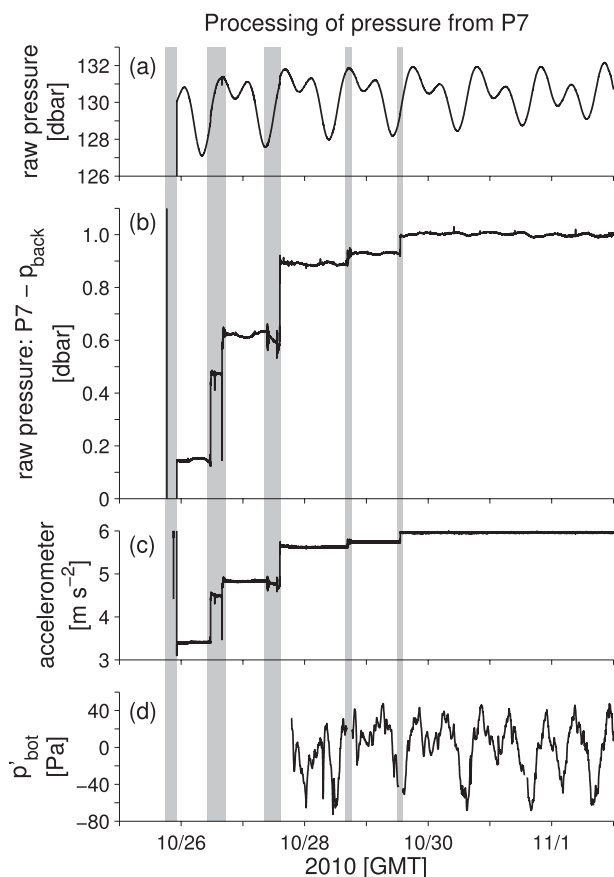
FIG. 3. (a) Raw pressure from P7. Periods of time where the Ppod was sinking or rolling are highlighted by the vertical gray bars. (b) The pressure difference between $p_{P7}$ and $p_{back} = 0.5(p_{L1} + p_{P1})$. The sinking or rolling of the instrument is clearly visible as abrupt changes in the pressure anomaly. (c) The first component of g force from the accelerometer within the Ppod. (d) The final bottom pressure anomaly after the sinking events had been corrected. Note that 1 dbar = $10^4$ Pa.

For example, potential vorticity conservation defines a barotropic pressure with $p = p(\rho)$ and a baroclinic pressure with gradients of density and pressure that are not parallel (Vallis 2006). For internal tides, Kelly et al. (2010) defines a baroclinic pressure anomaly that includes pressure fluctuations due to internal waves and has a zero vertical mean. Here, the use of "internal" and "external" pressures are used to highlight isopycnal and sea surface perturbations and are not equivalent to baroclinic and barotropic pressures.

To get the dynamic pressure anomaly $(p'_{bot})$ from the raw Ppod pressure the following steps are taken. We use P7 as an example because it was located on a very steep section of the topography and therefore prone to instabilities. The largest part of the Ppod pressure is the resting depth $[-\rho_0 gz$ in (5)], which is about 130 dbar for P7 (Fig. 3a). The resting depth is calculated as an average of the raw pressure from each Ppod over the exact same time period, ensuring that the same tidal height variations are included equally for each Ppod. The second biggest part of the pressure signal comes from the tidal height $[\rho_0 g\overline{\eta}$ in (5)], which has a range of 4 m. It is taken to be an average of the pressure from the two Ppods that were located far from the topography (L1 and P1). This avoids contamination of the background pressure with pressure perturbations occurring near the topography. The background stratification term $[g \int_z^{\eta} \overline{\rho}(z,t)\, dz$ in (5)] is not calculated explicitly because $\overline{\rho}$ is not known at every time step. However, it is accounted for indirectly when removing the background tidal signal because the pressures at L1 and P1 include changes in the background stratification in addition to changes in the sea surface height.

Distinct sinking events are visible in the Ppod pressure anomaly (Fig. 3b). These occurred when the autonomous Ppods shifted or rolled on the steep topographic slopes. P7 moved downward by about 1 m over the duration of the deployment. Acceleration records from within the Ppod confirm that the Ppod moves and changes orientation when pressure jumps occur (Fig. 3c). To fix these, the pressure anomalies before and after the sinking events are aligned by eye. At times when the pressure could not be aligned visually, parts of the record were discarded. For instance, in the case of P7, there were numerous sinking events before 28 October and the periods of time between the sinking events when the Ppod was stable were quite short, and the first 40 h of data were thus discarded.

Further treatment of the dynamic bottom pressure anomalies included removing spikes when necessary. All of the pressure anomalies were low-pass filtered with a 15-min Hanning window to remove high-frequency jaggedness and variability. After processing, the dynamic bottom pressure anomalies are 1000 times smaller than the raw pressure. Sources of error associated with calculating the bottom pressure anomalies are discussed in the appendix.

### b. Fluctuations of bottom pressure anomalies

When tides flow over and around TTP, the bottom pressure anomalies fluctuate (Figs. 4 and 5). Along the ridge transect, a difference can be seen in the size of $p'_{bot}$ from one side of the topography compared to the other. The two Ppods on the north side of the headland (Figs. 4b,c) have smaller anomalies and more erratic variability than the two on the crest (Figs. 4d,e) and the two on the south side of the headland (Figs. 4f,g). The flood tides are faster than ebbs (Fig. 4a) so larger pressure anomalies on the lee side of the topography during flood are expected. Furthermore, it is possible that the asymmetry of the
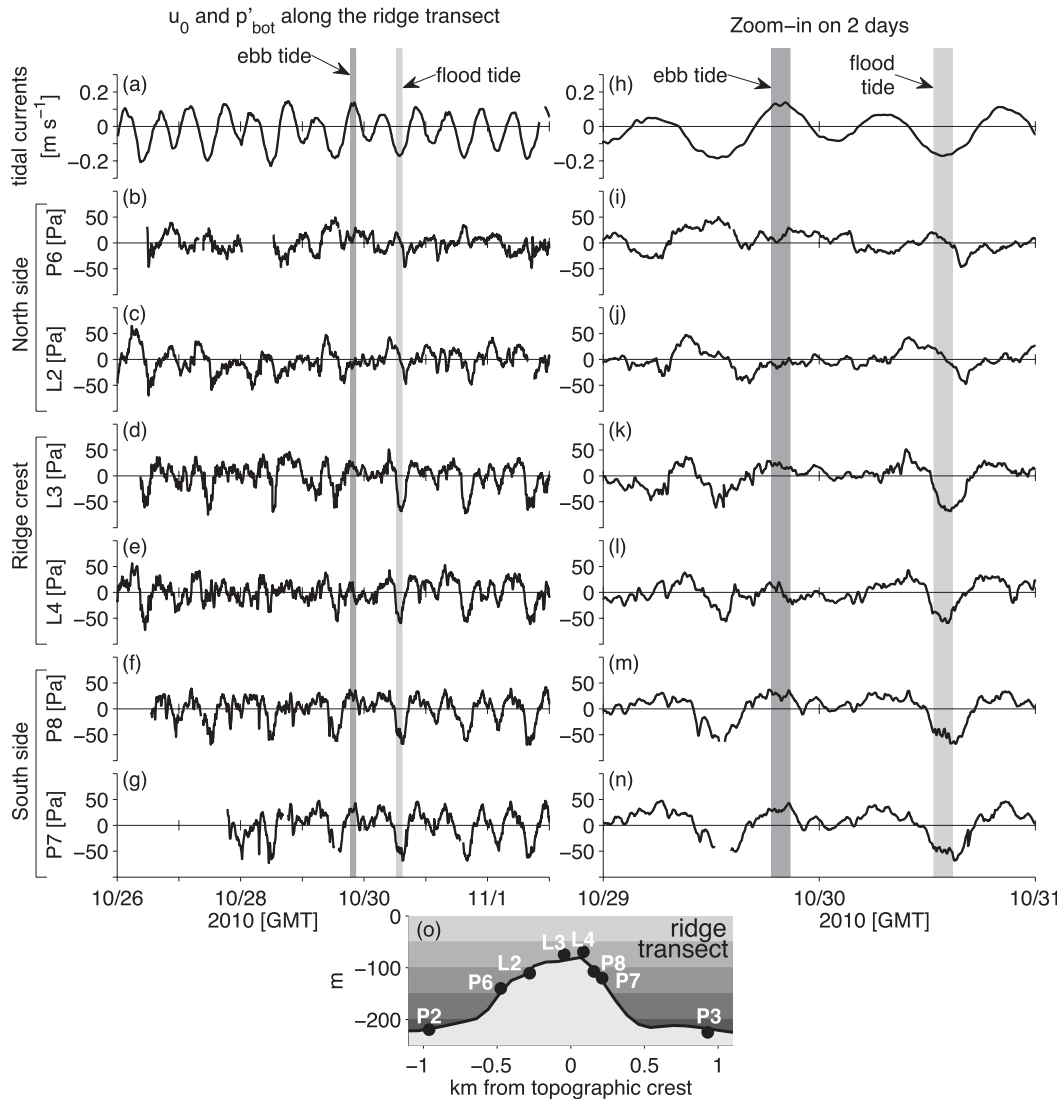
FIG. 4. (a),(h) Tidal currents ($u_0$). Bottom pressure anomalies from the Ppods ($p'_{bot}$) located along the ridge transect, arranged from north to south for (b)–(g) the entire week-long deployment and (i)–(n) a zoom-in on two days. The dark (light) gray vertical line shows the time from one hour before to one hour after maximum ebb (flood) tide. (o) The locations of the Ppods.

headland topography itself—the south side is steeper than the north side—augments this difference in the magnitude of $p'_{bot}$.

Repeated patterns of highs and lows that correspond to the tidal currents are visible in the zoomed-in view of $p'_{bot}$ (Figs. 4i–n). The light gray vertical bar highlights a two-hour window spanning maximum flood tide. The Ppods at the ridge crest and on the south (downstream) side of the topography show negative $p'_{bot}$ with magnitudes greater than 50 Pa (Figs. 4k–n). The negative anomaly starts at least an hour and a half before maximum flood tide and extends for another two or more hours after maximum flood tide. This low pressure is due

to a lee wave that forms on the south side of the topography and is only released when the tides have slackened sufficiently (detailed in section 5). Pressure anomalies on the north (upstream) side of the headland are essentially zero throughout the same time period. This difference in pressure across the topography is what creates form drag. The pattern of bottom pressure anomalies during ebb tide is the opposite of flood (dark gray vertical bar in Fig. 4). On the north (downstream) side of the headland and at the headland crest $p'_{bot}$ is nearly zero, and on the south (upstream) side $p'_{bot}$ is positive. The smaller pressure anomalies during ebb mean less form drag than during flood. Similar patterns of pressure anomalies are
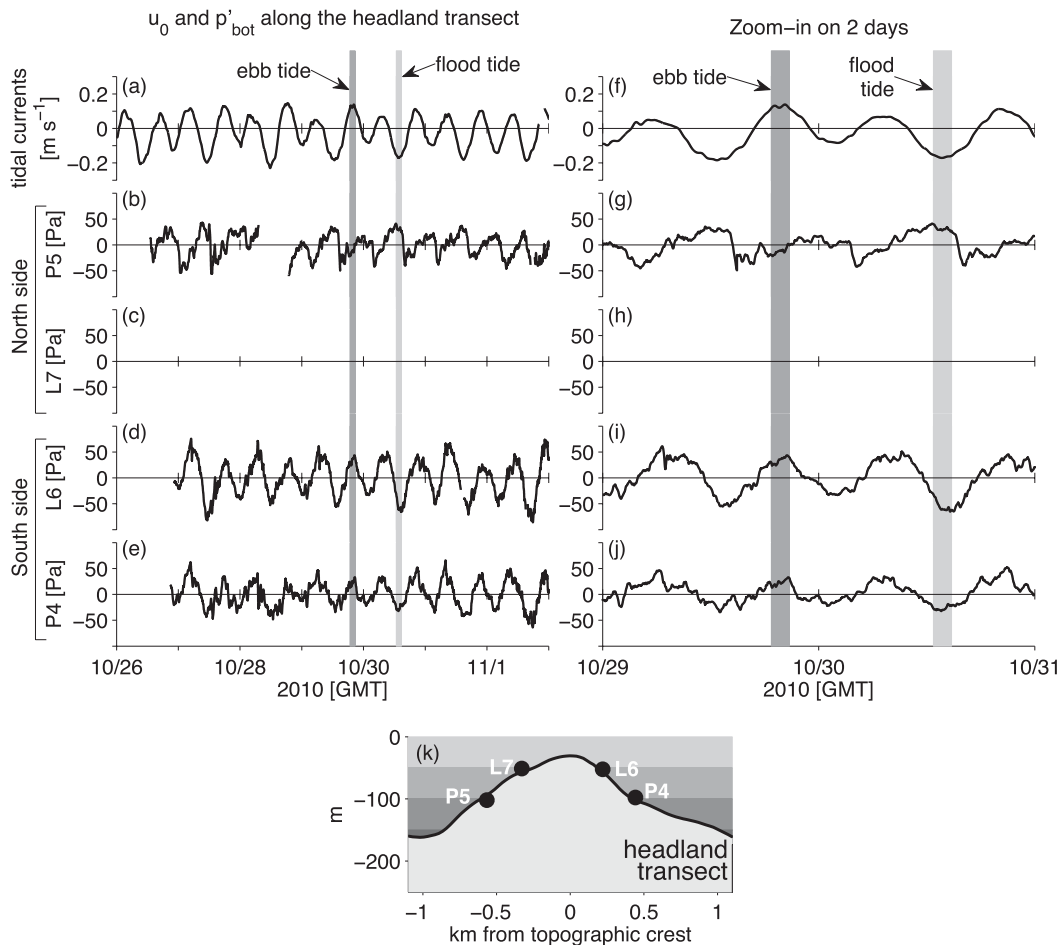
FIG. 5. (a),(f) Tidal currents ($u_0$). Bottom pressure anomalies from the Ppods ($p'_{bot}$) along the headland transect, from north to south for (b)–(e) the entire week-long deployment and (g)–(j) a zoom-in on two days. The dark (light) gray vertical line shows the time period extending from one hour before to one hour after maximum ebb (flood) tide. (c),(h) The Ppod on lander 7 failed. (k) Locations of the Ppods.

seen along the headland transect (Fig. 5) with high pressure on the upstream side and low pressure on the downstream side of the topography.

When $p'_{bot}$ from each Ppod along the ridge transect is plotted versus along-channel distance (Fig. 6), it is evident that the pressure anomaly is consistently positive on the upstream side and negative on the downstream side of the topography. Here, $p'_{bot}$ from each Ppod is averaged over a 2-h window spanning maximum tidal currents, and then the mean and 95% confidence intervals (Emery and Thomson 2004, section 3.8.2) are calculated for the 7 strong flood tides, 6 weak flood tides, 13 ebb tides, 14 slack tides between flood and ebb, and 13 slack tides between ebb and flood. During strong floods the difference in pressure across the topography is largest with a nearly 80 Pa drop from north to south (Fig. 6a). There is also no background slope to the sea surface ($\eta_{tilt}$) because the pressure at the far-field Ppods is near zero.

The mean pressure decreases slightly in the along-channel direction during weak floods, but not enough to be statistically significant (Fig. 6b). There is an along-channel increase in $p'_{bot}$ during ebb tides, which is statistically significant (Fig. 6c). During slack tides, the pressure change near the topography is small, whereas the along-channel sea surface tilt ($\eta_{tilt}$) is visible from the difference in pressure at the far-field Ppods. The sea surface tilt due to tidal acceleration, calculated with Eq. (11) (section 8), is shown to compare closely to the pressure anomalies measured by the Ppods during slack tides (Figs. 6d,e).

## 4. Form drag from bottom pressure

### a. Total form drag

Form drag ($D_{form}$) is calculated from $p'_{bot}$ using (1). Since the bottom pressure was only known in a few discrete

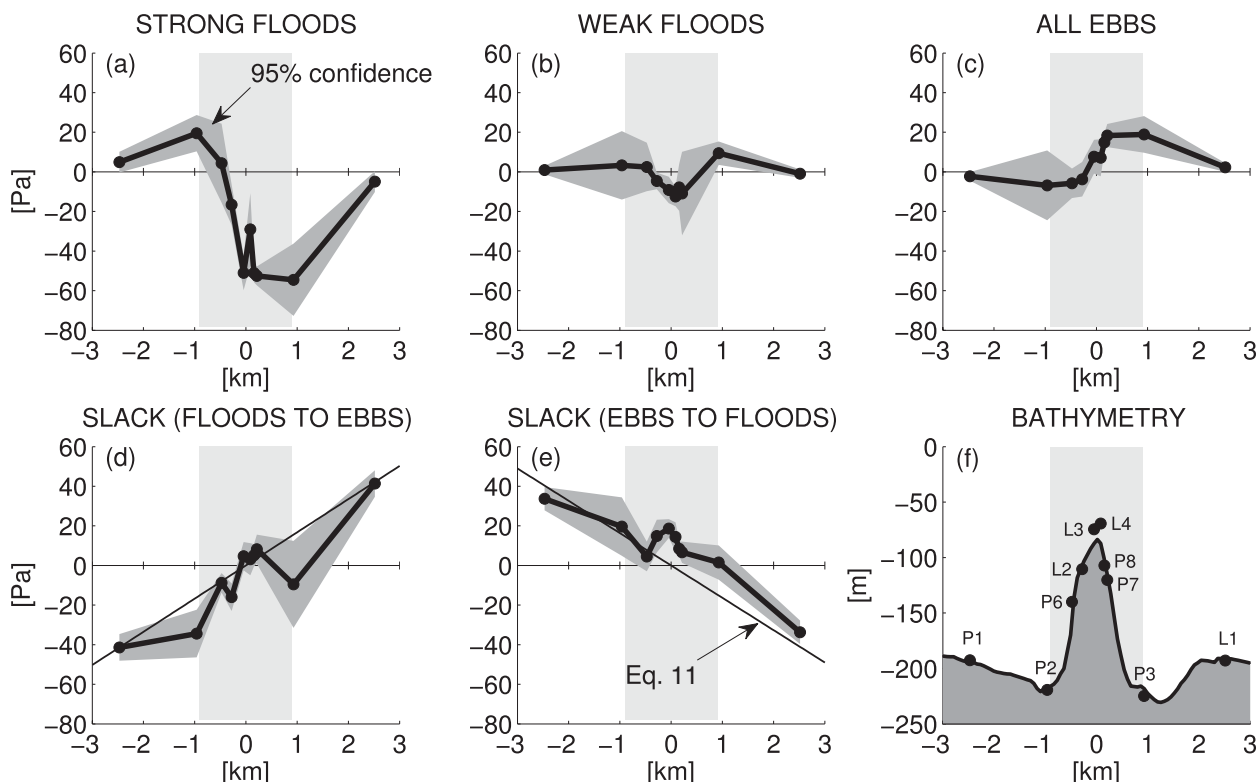Pressure anomalies along the ridge transect



FIG. 6. Average $p'_{bot}$ at Ppod locations along the ridge transect during (a) strong flood tides, (b) weak flood tides, (c) ebb tides, (d) slack tides between flood and ebb tides, and (e) slack tides between ebb and flood tides. The 95% confidence intervals are shown in dark gray. The thin black lines in (d) and (e) show the sea surface tilt calculated from the tidal acceleration with (11). (f) The along-channel position of the Ppods in relation to the bathymetry. The light gray shading behind all of the subplots shows the region where the topography has a nonzero slope.

locations, three independent ways of calculating the integral in (1) were attempted and shown to converge (appendix). Peak form drag occurs during the strong flood tides as highlighted for one tide with the vertical gray line (Figs. 7b,e). Along the both transects, maximum $D_{form}$ has a magnitude of $1 \times 10^4$ N m$^{-1}$.

Large peaks in power [$P_{form}$, (2)] occur during the strong flood tides with values as large as $2 \times 10^3$ W m$^{-1}$ for both the ridge and headland transects (Figs. 7c,f). The tidally averaged $P_{form}$ along the ridge and headland transects is 248 W m$^{-1}$ and 357 W m$^{-1}$, respectively. The fact that $P_{form}$ along both transects is relatively similar suggests that internal waves that are generated along the ridge transect and eddies that are generated along the headland transect contribute nearly equally to the total energy removed from the tides by TTP. The power per unit area ($P_{form}/L$) can be found by dividing the power by the transect lengths ($L$), which are 1.2 and 1.9 km along the ridge and headland transects, respectively. Average $P_{form}/L$ is found to be approximately 0.2 W m$^{-2}$ along both transects. Multiplied by a topographic area

$A_0 = 2.5$ km$^2$, an estimate for total ($P_{form}/L)A_0$ is 0.5 MW. Edwards et al. (2004) use a numerical model to estimate the work rate at TTP to be 0.72 MW. One reason for the difference between these two estimates is because this experiment was done during neap tides when there was a weak and a strong flood tide each day. During the Edwards et al. (2004) experiment, there were two strong floods each day. Since most of the drag and power loss occur during strong floods, the average power loss could double from 0.5 to 1.0 MW when there are twice as many strong flood tides. Furthermore, during spring tides, currents are faster which would also lead to an increased power loss.

To put the tidally averaged estimate of ($P_{form}/L)A_0 = 0.5$ MW into context, it can be compared to the tidal energy flux calculations made by Lavelle et al. (1988) throughout Puget Sound. They estimated that the total tidal energy flux into Puget Sound is 733 MW, of which 5 MW are dissipated in East Passage, the region of Puget Sound where TTP is located. Therefore, energy losses at TTP contribute 10% of the total losses in East Passage even though the area of TTP is only 0.6% of the total area of East Passage.
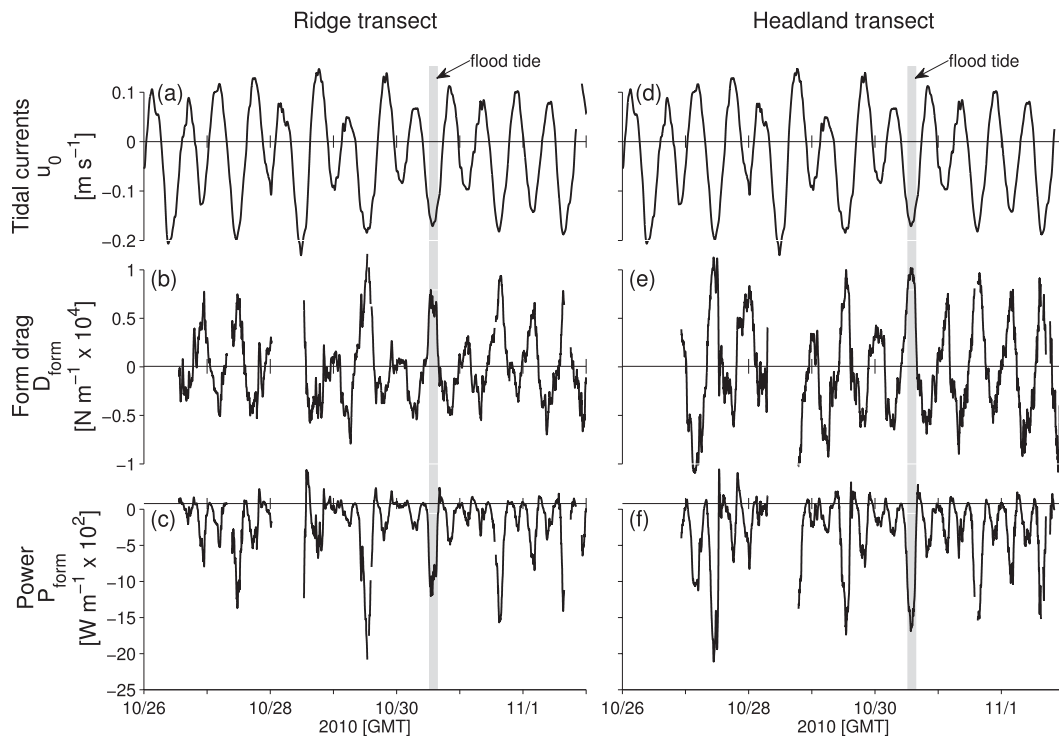
FIG. 7. (a),(d) Tidal velocity ($u_0$). (b),(e) Form drag ($D_{form}$), which has the opposite sign as the tidal currents because it is a force that opposes the flow. (c),(f) Power ($P_{form}$), which is negative because energy is being lost from the tidal currents through form drag. One of the flood tides is highlighted with the vertical gray bar. Both the ridge in (b),(c) and headland in (e),(f) transects show large $D_{form}$ and $P_{form}$ during strong flood tides.

### b. Form drag from the shallow water momentum equation

In the previous section, $D_{form}$ was integrated across the topography directly from $p'_{bot}$. In this section, drag will again be calculated, but in a more indirect way that involves finding the drag coefficient from the shallow water momentum equation. We refer to this as the "bulk drag" ($D_{bulk}$) as it includes both form drag and frictional drag.

To calculate $D_{bulk}$, start with the linear, shallow water momentum equation in the along-channel direction with depth-integrated friction (Officer 1976, sections 3–4),

$$\frac{\partial u}{\partial t} - fv = -g\frac{\partial \eta}{\partial x} - \frac{C_D u|u|}{H}. \tag{7}$$

Assume no cross channel flow ($v = 0$ m s$^{-1}$) and an average depth ($H = 200$ m). Since this is a bulk calculation, use the background tidal velocity ($u_0$) for $u$, and calculate the sea surface height gradient with the two far-field Ppods (L1 and P1). We solve (7) algebraically at every time step for the drag coefficient $C_D$ and then find an average drag coefficient over times when the magnitude of the velocity is greater than 0.1 m s$^{-1}$. This

results in an average drag coefficient of $C_D = 9 \times 10^{-2}$, which is very large—about 30 times larger than the canonical frictional drag coefficient of $3 \times 10^{-3}$. However, this is not surprising because $C_D$ includes both frictional and form drag at a location where form drag is substantially larger than frictional drag.

Using the drag coefficient $C_D = 9 \times 10^{-2}$, $D_{bulk}$ can be calculated using a quadratic drag law

$$D_{bulk} = \frac{1}{2}\rho_0 C_D (x_{L1} - x_{P1}) u_0 |u_0|, \tag{8}$$

where $x_{L1}$ and $x_{P1}$ are the along-channel positions of the Ppods at the end of the domain. Here, $D_{form}$ and $D_{bulk}$ were calculated with completely different instruments and methods, but nonetheless they give quite similar results (Fig. 8). They have nearly identical magnitudes during flood and large ebb tides. During weak ebbs when the velocity is less than 0.1 m s$^{-1}$, $D_{bulk}$ misses some peaks. Bulk power ($P_{bulk}$) is the product of $D_{bulk}$ and $u_0$. Average $P_{bulk}$ is 304 W m$^{-1}$, which agrees with average $P_{form}$ along the ridge and headland transects of 248 and 357 W m$^{-1}$, respectively. The frictional drag—calculated with a quadratic drag law and a drag coefficient of $C_D = 3 \times 10^{-3}$—has an average power of only
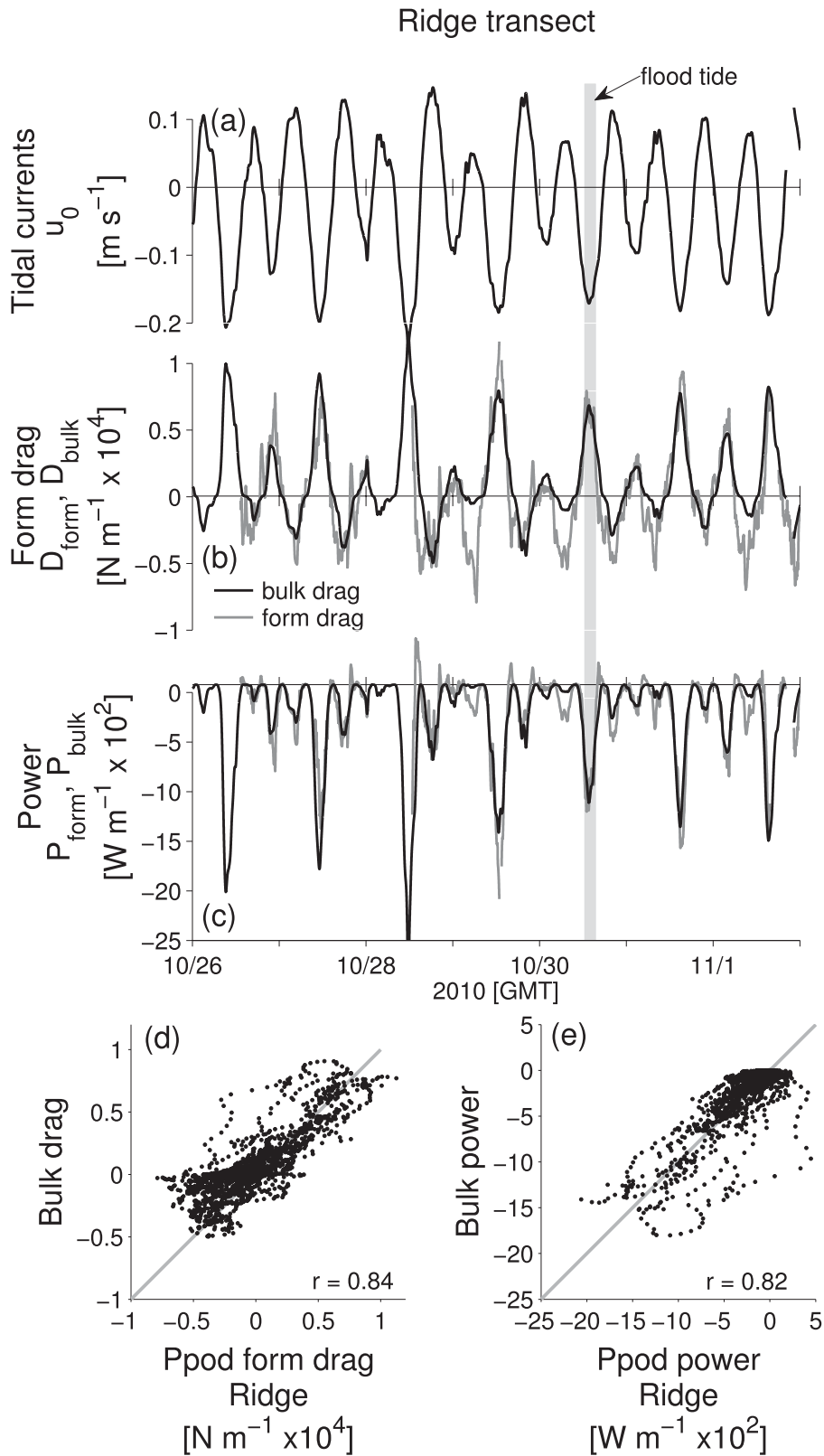
## Ridge transect



FIG. 8. (a) Tidal velocity ($u_0$), (b) $D_{form}$ along the ridge transect (gray, same as in Fig. 7) and $D_{bulk}$ (black), (c) $P_{form}$ (gray) and $P_{bulk}$ (black), (d) scatterplot of $D_{form}$ vs $D_{bulk}$, and (e) scatterplot of $P_{form}$ vs $P_{bulk}$.

10 W m$^{-1}$ so comparing $D_{bulk}$ to $D_{form}$ is a legitimate comparison. Despite some scatter, when $D_{form}$ and $P_{form}$ are plotted versus $D_{bulk}$ and $P_{bulk}$ most of the data falls along the 1:1 line (Figs. 7d,e).

The equivalence between $D_{form}$ and $D_{bulk}$ gives us confidence that our estimates of $D_{form}$ are accurate. These are two independent measurements that employed different instruments and theory, but nonetheless the correlation of form drag and power between the two methods—especially during strong flood tides—is high.

## 5. Bottom pressure and form drag from potential density

### a. Internal lee waves

As a comparison to the bottom pressure ($p'_{bot}$) and form drag ($D_{form}$), we calculate internal pressure anomaly ($p'_{int}$) and internal form drag ($D_{int}$) from the Chameleon transects of potential density. It gives a representation of whether the isopycnals are raised or lowered in particular parts of the domain during certain times in the tide. First, the potential density is interpolated to a regular spatial grid. Unlike, for $p'_{bot}$ where the background stratification in (5) was ignored, here it is calculated by averaging the density profiles from deep casts located far from the topography. The density anomaly ($\rho'$) is simply the difference between the Chameleon density ($\rho$) and the background density ($\rho_0 + \overline{\rho}$). Then, pressure is calculated using the hydrostatic equation,

$$\frac{\partial p'_{int}}{\partial z} = -\rho' g, \qquad (9)$$

assuming zero pressure at the surface. The pressure anomaly in the deepest grid box is taken to be the internal bottom pressure anomaly, $p'_{int}$.

Sections of potential density along the ridge transect for one full tidal cycle show lee waves on the downstream side of the topography (Fig. 9). Associated with these lee waves are negative $p'_{bot}$ and $p'_{int}$. In this figure, $p'_{bot}$ was averaged over the time period of the Chameleon transect, which was approximately one hour long.

Examining the density and bottom pressure anomalies over a tidal cycle (Fig. 9) shows the evolution of the internal lee waves. The sequence starts at the very end of a small flood tide (Fig. 9a) when the tidal velocity is nearly zero. At this time, $p'_{bot}$ is nearly zero and there is a slight tilt of the isopycnals with higher $p'_{int}$ on the south side. At time 2 (Fig. 9b), the currents have started to ebb (flow to the north). There is slightly higher $p'_{bot}$ on the south side of the headland (P8 and P7), but there is little change in the density field. At time steps 3 and 4 (Figs. 9c,d), the flow is strongly ebbing and the isopycnals show

a lee wave that is situated above the topography just to the north of the topographic crest. At both of these time steps, $p'_{bot}$ shows a higher pressure on the upstream side of the topography (L4, P8, and P7) than on the downstream side (P6 and L2). There is a discrepancy between $p'_{bot}$ and $p'_{int}$, which is likely due to sea surface height displacements that are accounted for by the Ppods but not by the density. By time step 5 (Fig. 9e), the ebb tide has slackened, although some residual signals remain.

Time steps 6 through 9 show flood tides (Figs. 9f–h). In time step 6, both $p'_{bot}$ and $p'_{int}$ are nearly zero. The large $p'_{int}$ at P2 is most likely caused by a sea surface height perturbation traveling away from the topography. In time steps 7 and 8 (Figs. 9g,h), there is a large pressure difference across the topography both from the Ppods and potential density. Just as was seen in Fig. 4, the two Ppods on the crest of the topography (L3 and L4) and the two on the downstream side (P8 and P7) all have large negative $p'_{bot}$ at maximum flood tide. Internal lee waves can be seen in the potential density section. By time step 9 (Fig. 9i), the flood tide has slackened. At time step 10 (Fig. 9j), the tide has begun to ebb again and the cycle will repeat itself. Throughout the experiment, similar patterns to these 10 time steps are seen at flood, ebb, and slack tides.

Differences between $p'_{bot}$ and $p'_{int}$ in Fig. 9 are expected. The Ppods include external and nonhydrostatic pressure perturbations whereas the Chameleon density does not. In particular, sea surface perturbations due to eddies are measured to be as big as 200 Pa by McCabe et al. (2006), therefore, differences between $p'_{bot}$ and $p'_{int}$ would occur when eddies cross the ridge transect. Much smaller errors could arise because the Chameleon density profiles only go to 160 m, missing as much as 40 m of the water column in the deep parts of the transect. Time variability may also create small differences. In Fig. 9, $p'_{bot}$ has been averaged over the hour it took to complete the transect, whereas each individual Chameleon profile takes only 5–10 min.

### b. Form drag from potential density

The internal form drag ($D_{int}$) and power ($P_{int}$) can be calculated from $p'_{int}$ (Fig. 10). A continuous integration method (appendix) is used to integrate $p'_{int}$ across the topography.

On the ridge transect, $D_{int}$ and $P_{int}$ peak during strong flood tides just as seen for $D_{form}$ and $P_{form}$. The tidally-averaged $P_{int}$ is 209 W m$^{-1}$, which accounts for about 80% of $P_{form}$ along the ridge transect (248 W m$^{-1}$). Scatterplots of $D_{form}$ and $P_{form}$ versus $D_{int}$ and $P_{int}$ (Figs. 10g,h) show a good correlation between the two datasets. However, the strong correlation between $D_{form}$ and

Potential density anomalies and p'$_{bot}$ along the ridge transect throughout one tidal cycle
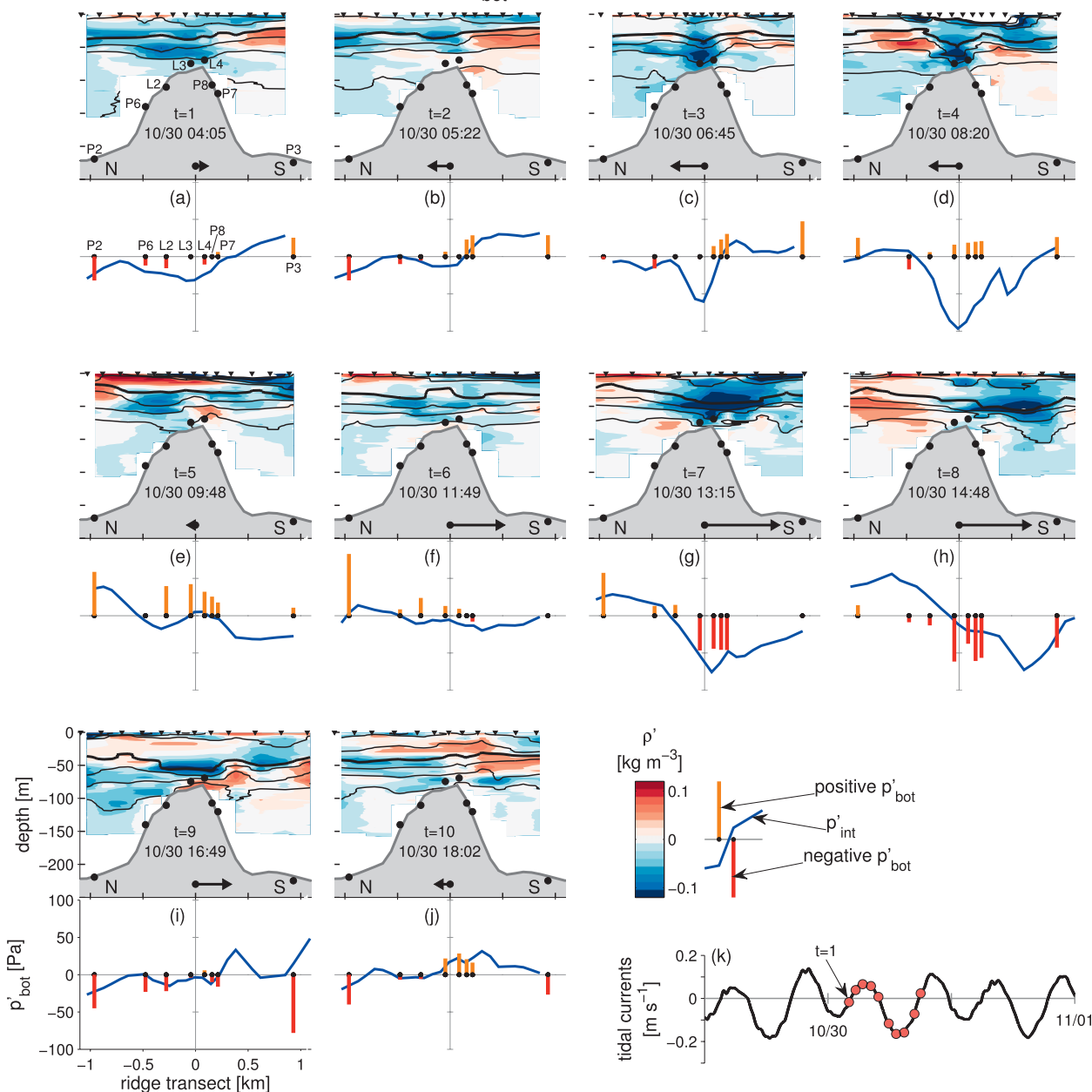


FIG. 9. (a)–(j) (top) Potential density anomalies (red/blue gradient) overlaid with contours of density at intervals of 0.1 kg m$^{-3}$ with the 1023 kg m$^{-3}$ isopycnal in bold. Also shown are Ppods (black dots), Chameleon drops (black triangles), and tidal currents (black arrows). (a)–(j) (bottom) $p'_{bot}$ and $p'_{int}$. (k) Tidal currents highlighting the 10 time-steps (red dots).

$D_{int}$ only exists during flood tides ($r = 0.79$ during flood tides, $r = 0.29$ during ebb tides).

Along the headland transect, a CTD was used to collect density data at four stations along the transect. This was not enough spatial coverage to resolve isopycnal height variations. Here, $D_{int}$ and $P_{int}$ do not correlate with $D_{form}$ and $P_{form}$ (Figs. 10e,f,i,j). This discrepancy highlights the importance of a CTD that continually

samples like the Chameleon profiler. A sensitivity test was performed to determine how many CTD casts are necessary to get an accurate estimate of $D_{int}$ by subsampling the Chameleon profiles. For instance, if only half the Chameleon casts are used to calculate $D_{int}$, the results are essentially the same as if every cast is used. However, if every fourth cast is used, the results start to deviate, and if fewer are used, the results become
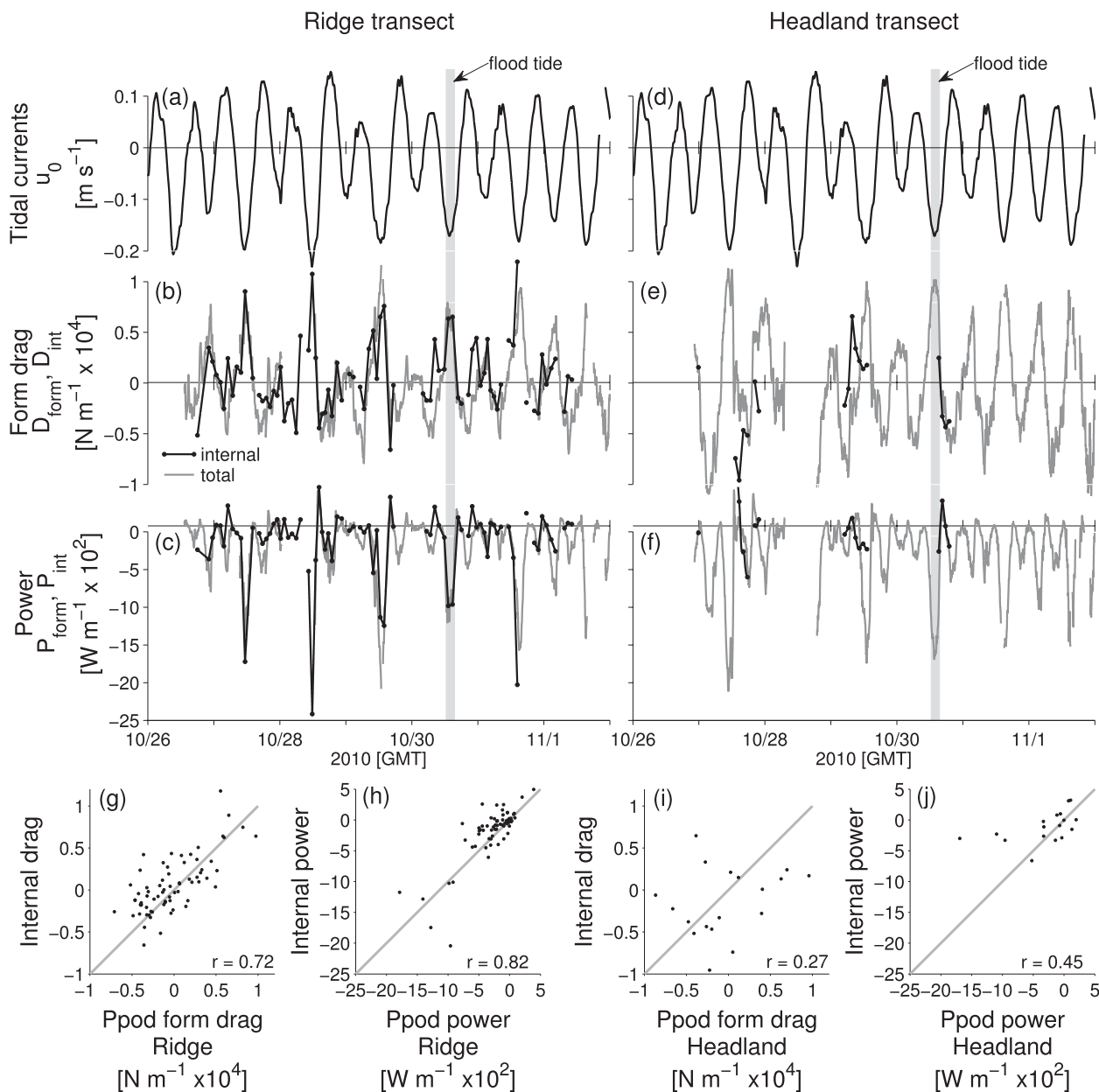
FIG. 10. (a),(d) Tidal velocity ($u_0$). (b),(e) $D_{form}$ (gray) and $D_{int}$ (black) along the ridge in (b) and headland in (e) transects. Each Chameleon transect is indicated with a black dot. (c),(f) $P_{form}$ (gray) and $P_{int}$ (black). (g)–(j) Scatterplots comparing $D_{int}$ to $D_{form}$ in (g),(i) and $P_{int}$ tp $P_{form}$ in (h),(j) along the ridge in (g),(h) and headland in (i),(j) transects.

meaningless. It also matters where the casts are taken. If a cast is made in the middle of an internal wave, the results will be good, but if big features like that are missed, the final result could be erroneous.

## 6. Turbulent kinetic energy dissipation rate

The Chameleon profiler also measures turbulent kinetic energy dissipation rate (Fig. 11). During both flood (Figs. 11f–h) and ebb tides (Figs. 11c,d), increased

dissipation is seen on the lee side of the topography. Maximum energy dissipation rates of $5 \times 10^{-5}$ W kg$^{-1}$ were measured during peak flood tides (Fig. 11g). The dissipation is quite patchy. It was found that 90% of the dissipation occurs in only 20%–30% of the volume. The microstructure measurements show dissipation at nearly all depths. This is evidence that unlike frictional drag, which only dissipates energy in the bottom boundary layer, form drag dissipates energy throughout the water column.
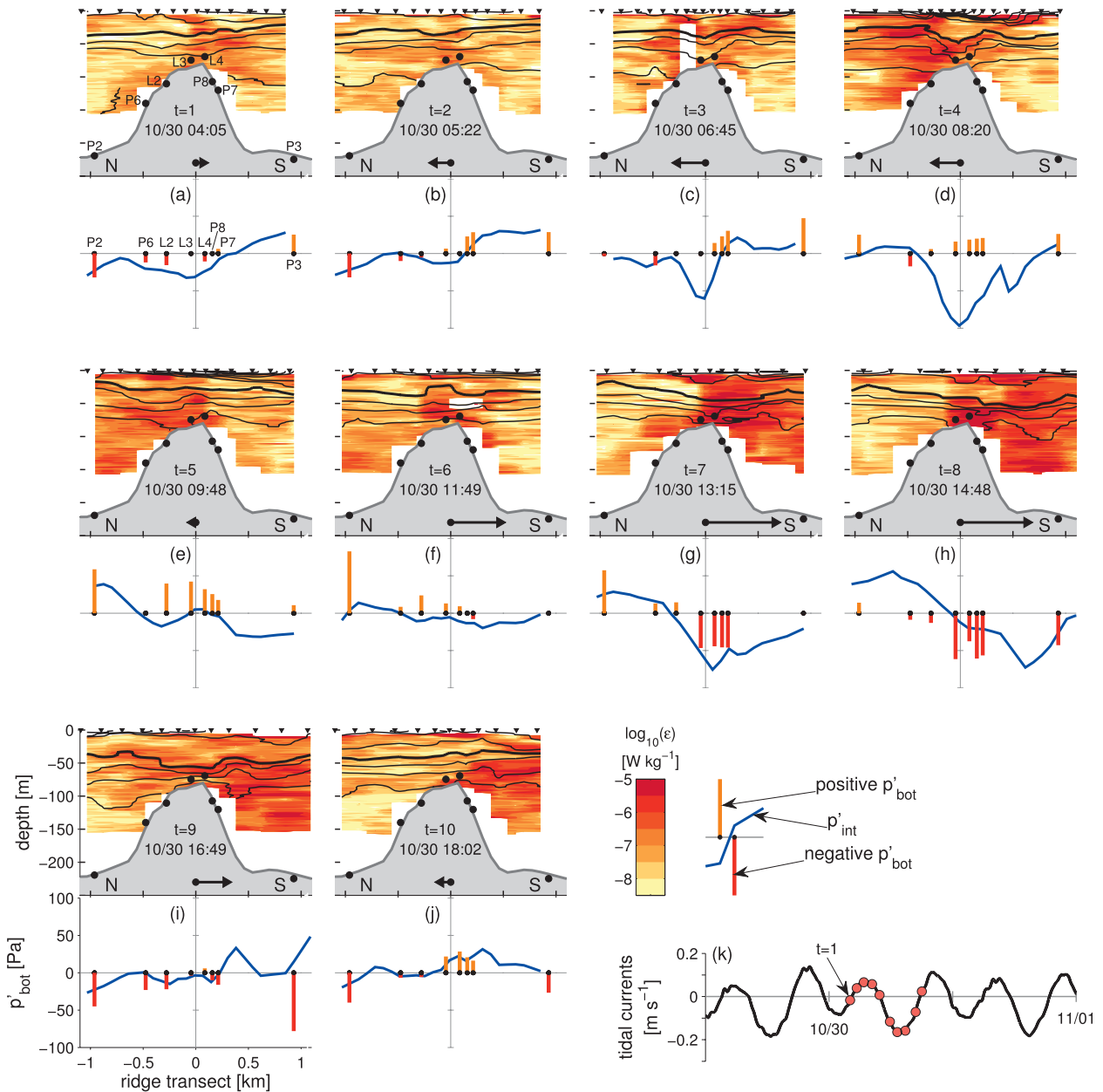
FIG. 11. (a)–(j) (top) Turbulent kinetic energy dissipation rate (red/orange gradient) at the same times as Fig. 9. Isopycnals are shown with black contours at intervals of 0.1 kg m$^{-3}$ with the 1023 kg m$^{-3}$ isopycnal in bold. (a)–(j) (bottom) $p'_{bot}$ and $p'_{int}$ (Fig. 9). (k) Tidal currents highlighting the 10 time-steps (red dots).

Dissipation can be spatially integrated along the ridge transect at each time step and compared to $P_{form}$ (Fig. 12a). There are distinct peaks of $P_{form}$ at flood tides, whereas peaks in dissipation rate are not nearly as large. This discrepancy is also visible when viewed as a scatterplot (Fig. 12b). At peak floods, the spatially integrated dissipation is only 25%–50% of the total power. Assuming that our turbulence observations have

adequately captured the total dissipation, this suggests that not all of the energy is dissipated locally, but instead is carried away from the topography by either eddies (McCabe et al. 2006; Canals et al. 2009) or internal waves (section 5a) that do not break directly above TTP. The percentage of local energy dissipation at TTP can be compared to other sites such as Knight Inlet where Klymak and Gregg (2004) found that one-third of the energy lost
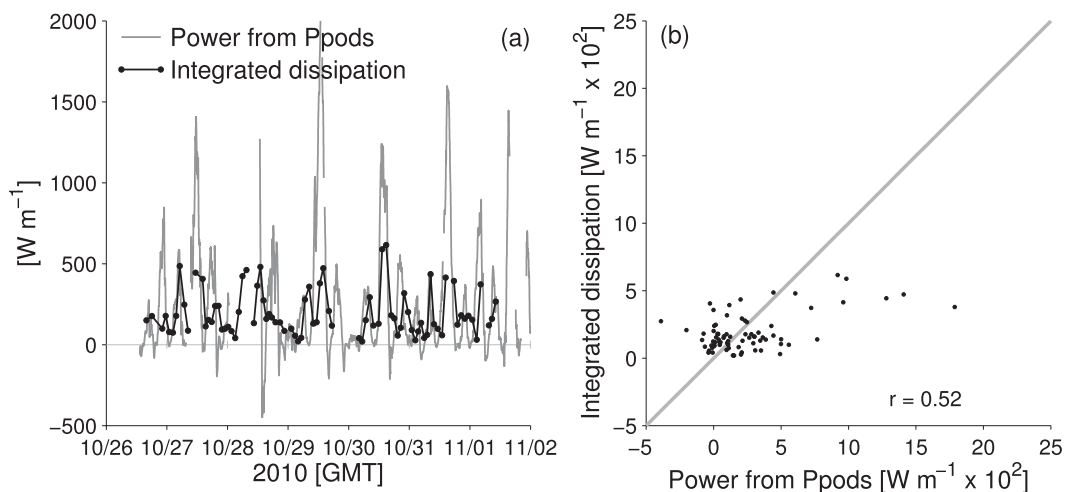
FIG. 12. (a) Spatial integral of turbulent kinetic energy dissipation rate (black line and dots) compared to $P_{form}$ (gray line, negative of Fig. 7c). (b) Scatterplot comparing $P_{form}$ (x axis) to the integrated dissipation (y axis).

from the barotropic tides is dissipated near the sill while the rest radiates away, and to the entrance sill in Loch Etive where Inall et al. (2005) found that three quarters of the energy is radiated away by internal waves and a horizontal eddy and only a quarter is dissipated locally.

## 7. Velocity surveys

Shipboard and bottom lander ADCP velocities were collected along the two transects (Fig. 13). At ebb tide (Fig. 13a), the tidal current ($u_0$) flows from the SSE. Along the ridge transect, the currents on the south side of the headland are deflected toward the center of the channel by the topography, and on the headland transect, the currents are even deviated somewhat southward. Currents reach speeds of 0.5 m s$^{-1}$ on the south side of the topography, with the strongest velocities at 20-m depth. On the north side of the topography during ebb tide, the currents are weak. The velocities close to TTP are much faster than tidal currents in the center of
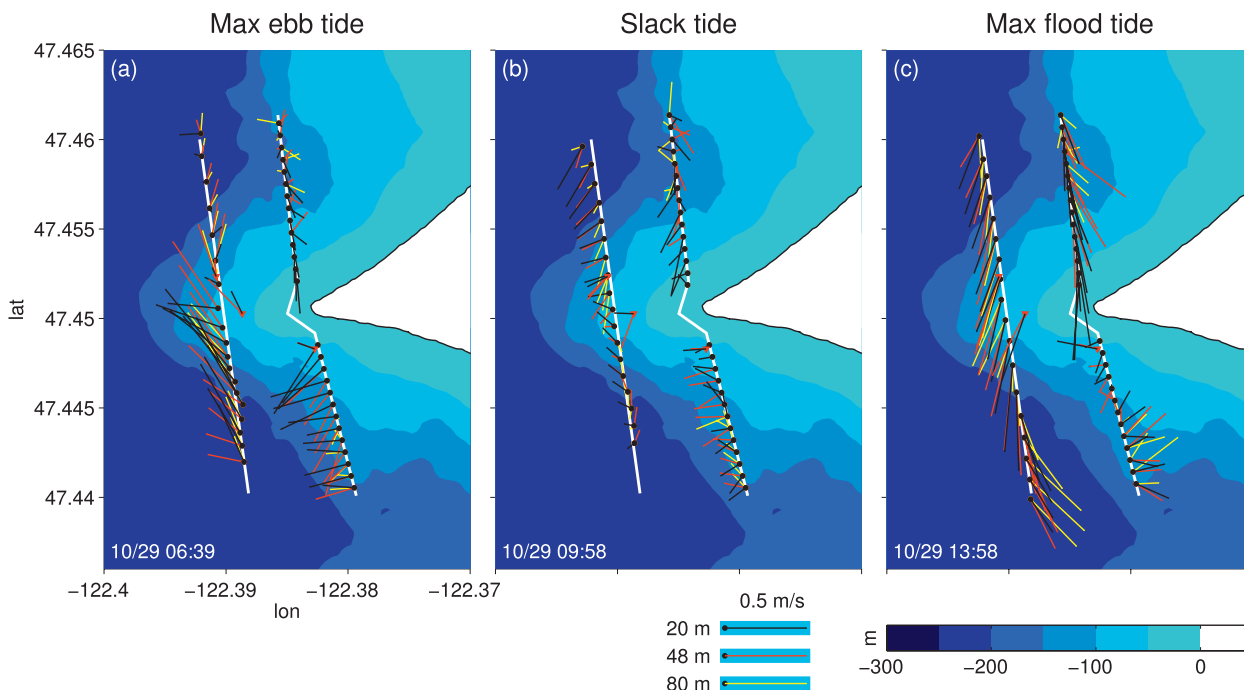


FIG. 13. Plan views of velocity at three depths (20, 48, and 80 m) at (a) maximum ebb, (b) slack, and (c) maximum flood tides.

the channel which reach speeds of only 0.2 m s$^{-1}$ during the strongest flood tides.

The currents near TTP never completely stop due to the presence of lingering eddies and other local dynamics. At slack tide (Fig. 13b), the currents are weaker than those at flood or ebb, but are still nearly 0.2 m s$^{-1}$ which is as fast as $u_0$ at maximum flood.

At flood tide (Fig. 13c) when the background current is flowing from the NNW, the currents near TTP are strongly influenced by the topography. On the north side of the headland along the ridge transect, the currents are deflected toward the center of the channel at all depths. On the south side of the topography, a counterclockwise rotating eddy is evident (Fig. 13c). At the very south ends of the two transects, the currents are flowing strongly to the east. Just south of the tip of TTP along the headland transect, the currents are flowing back toward the west. The sea surface height deformation associated with this eddy can be estimated. For simple, rotational flow, the frictionless, steady shallow water momentum equation can be written in polar coordinates as,

$$-\frac{u_\theta^2}{r} - f u_\theta = -g \frac{\partial \eta}{\partial r}, \tag{10}$$

where $u_\theta$ is the angular velocity, $r$ is the radius of the eddy, and $\partial \eta / \partial r$ is the gradient of sea surface height in the radial direction. Assuming $u_\theta \approx 0.3$ m s$^{-1}$ at $r \approx 500$ m, the sea surface height difference between the center of the eddy and the edge is 10.5 mm (105 Pa), with the center being lower than the edge. On the north side of the headland where the eddy spins in the clockwise (anticyclonic) direction, the sea surface height deformation would be only 7.5 mm because the Coriolis force term has the opposite sign as the centripetal acceleration term. These sea surface deformations are of the same order of magnitude as $p'_{\text{bot}}$.

## 8. Inertial pressure and form drag

WM09 showed that when the flow is unsteady, form drag is not only created by the generation of internal waves and eddies, but it is also created by the oscillatory nature of the flow. They referred to this part of the form drag as the inertial drag.

We can gain insight into the inertial part of the pressure field by thinking about potential flow (Dean and Dalrymple 1984). By definition, steady potential flow does not create form drag because it is reversible; there is no flow separation. Oscillatory potential flow is also reversible. However, time-varying flows require pressure gradients to accelerate the flow, and these create an apparent form drag when they occur over sloping bottom topography. At flood and ebb tides, the sea surface is essentially flat, whereas at slack tide, the sea surface is sloped downward in the direction of tidal acceleration. This creates a pressure difference across the topography that results in form drag even without flow separation. We term this "inertial drag" ($D_{\text{inert}}$), which is most important in cases where the tidal excursion distance is nearly the same as the topographic length (WM09). It should be noted that the sea surface slope is related to the acceleration of the flow and not when high and low tides occur. Therefore, the theory for inertial drag is the same whether the estuary has a tidal wave that is progressive or standing.

In this study, since the domain is only a few kilometers long, the sea surface slope associated with tidal acceleration is assumed to be linear. The sea surface height at a given location can be calculated from the tidal acceleration [WM09, Eq. (15)]:

$$\eta_{\text{tilt}}(x,t) = \frac{1}{g} \frac{\partial u_0}{\partial t} (x - x_0), \tag{11}$$

where $x_0$ is a reference location, and $x$ is the along-channel distance from the reference location. To calculate $p'_{\text{inert}}$, (11) can be substituted into (6). It makes most sense to choose the reference location at the center of the topography, however, when calculating form drag using (1), as long as the same reference location is always used, it does not matter where it is located. Alternately, if pressure sensors are deployed upstream and downstream of the topography in far-field locations that are not directly affected by internal lee waves and eddies, $\eta_{\text{tilt}}$ can be calculated from the along-channel pressure gradient:

$$\eta_{\text{tilt}}(x,t) = \frac{1}{\rho_0 g} \frac{p_A - p_B}{x_A - x_B} (x - x_0), \tag{12}$$

where $A$ and $B$ indicate locations of pressure sensors up- and downstream of the topography. The sea surface tilt from both the far-field Ppods (12) and the tidal acceleration (11) compare well during slack tides when the slope is maximum (Figs. 6d,e). We choose to define $\eta_{\text{tilt}}$ as in (11) so that the inertial form drag is in perfect quadrature with the velocity. Therefore, even though $\eta_{\text{tilt}}$ creates form drag, it does not do tidally-averaged work on the flow. All of the form drag that does tidally-averaged work on the flow is contained within the external and internal pressure anomalies (6).

WM09 found that on headlands comparable to the size of TTP, the inertial form drag can be comparable in size to the form drag caused by flow separation. Therefore, it is important to calculate it in this oscillatory tidal case.
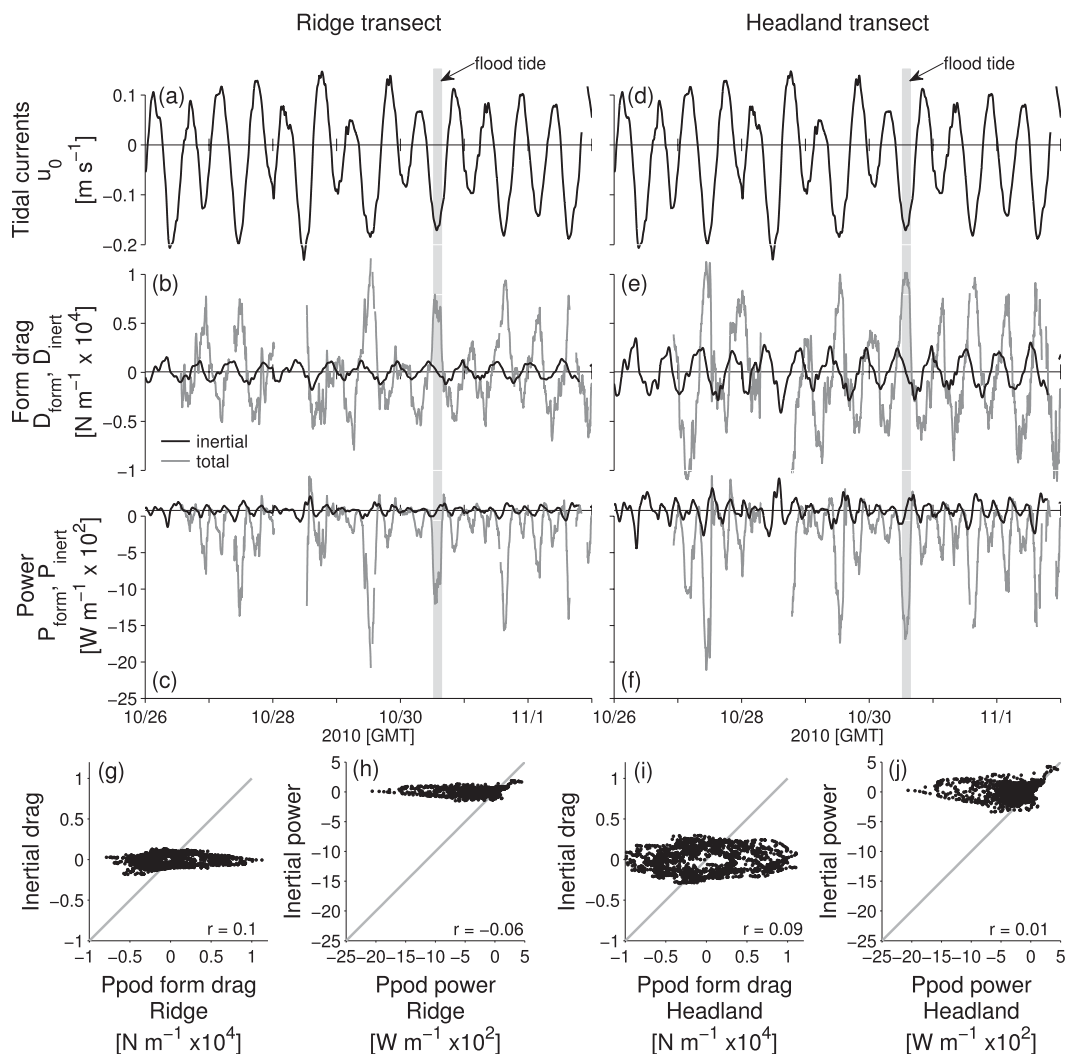
FIG. 14. (a),(d) Tidal velocity ($u_0$); (b),(e) $D_{form}$ (gray) and $D_{inert}$ (black); (c),(f) $P_{form}$ (gray) and $P_{inert}$ (black); and (g)–(j) $D_{form}$ and $P_{form}$ (x-axes) vs $D_{inert}$ and $P_{inert}$ (y-axes).

The local sea surface height associated with the background tilting of the sea surface is calculated at each Ppod location with (11). That height is converted to a bottom pressure anomaly using (6). Then $D_{inert}$ is calculated from (1) in the piecewise integration method (appendix). At maximum flood and ebb tides, $D_{inert}$ is zero, but at slack tide, when the acceleration is biggest, $D_{inert}$ has its maximum value (Fig. 14).

The amplitude of $D_{inert}$ is significantly smaller than the amplitude of $D_{form}$ along both the ridge (Fig. 14b) and headland transects (Fig. 14e). This contrasts the results of WM09, but was not entirely unexpected because their study was for headlands with vertical sidewalls, which is not the case for TTP. Inertial drag for a ridge is not expected to be as large as the inertial drag for a headland because the topographic slope ratio for a

ridge is usually only 1:10 (rise:run) whereas for a headland it is more like 1:1 (across-channel extent:along-channel extent). Therefore, since form drag is the product of pressure and slope, the inertial form drag will be less for a ridge than for a headland.

Most important, even though $D_{inert}$ and $P_{inert}$ are not zero, tidally averaged $P_{inert}$ *is* zero (Figs. 14c,f). The inertial drag does no net work on the flow. There is almost no correlation between $D_{inert}$ and $P_{inert}$ versus $D_{form}$ and $P_{form}$ along either transect (Figs. 14g–j).

## 9. Comparisons and parameterizations

TTP is complex because it generates both internal waves like a ridge and eddies like a headland as tidal currents flow over and around it. For the most part, in

oceanography, the flow dynamics over ridges and around headlands have been investigated separately.

For the headland case, WM09 found that the form drag on idealized headlands was well predicted by a bluff body drag law:

$$D_{\text{BB}} = \frac{1}{2}\rho_0 C_D h_0 u_0 |u_0|, \tag{13}$$

where $C_D$ is an $O(1)$ drag coefficient, and $h_0$ is the maximum topographic height. Bluff body drag is commonly used to estimate form drag on a wide variety of objects in nonstratified flow for which drag coefficients have been experimentally found (Fox and McDonald 1998, chapter 9).

Stratified flow over ridges is a complex problem that has been studied extensively. Gill (1982, chapters 6 and 8) and Baines (1995) explain variations of the steady case in their books. Garrett and Kunze (2007) review oscillatory flow over ridges in the deep ocean. They define a nondimensional parameter space that is based on the steepness

$$\left[ \varepsilon = kh_0 \left( \frac{\omega^2 - f^2}{N^2 - \omega^2} \right)^{-1/2} \right],$$

tidal excursion ($kU_0/\omega$), nonlinearity ($Nh_0/U_0$), and height ($\delta = h_0/H$). To get an idea of where TTP fits within this parameter space, the following physical dimensions are used: buoyancy frequency ($N = 6.25 \times 10^{-3}\,\text{s}^{-1}$), Coriolis frequency ($f = 1 \times 10^{-4}\,\text{s}^{-1}$), amplitude of the tidal velocity ($U_0 = 0.2\,\text{m s}^{-1}$), frequency of the M2 tides ($\omega = 1.4 \times 10^{-4}\,\text{s}^{-1}$), water depth ($H = 200\,\text{m}$), and height of the topography along the ridge transect ($h_0 = 115\,\text{m}$). For an isolated ridge like TTP, we follow Legg and Huijts (2006) and define the topographic wavenumber as $k = 1/L_0 = 2.5 \times 10^{-3}\,\text{m}^{-1}$ where $L_0 = 400\,\text{m}$ is the Gaussian $e$-folding length of the topography. It is found that TTP has a steepness parameter of $\varepsilon = 18$, which means the topographic slope is supercritical with respect to the wave ray slope. The tidal excursion parameter $kU_0/\omega = 3.6$, which means that the flow in this region is likely to produce quasi-steady lee waves. The nonlinear parameter $Nh_0/U_0 = 3.6$, which means that the flow over TTP could be blocked by the topography. Finally, the height parameter $\delta = 0.57$, which means that the topography occupies over half of the water column at the crest of the ridge. Along the headland transect, $\varepsilon = 18$, $kU_0/\omega = 2.4$, $Nh_0/U_0 = 4.7$, and $\delta = 0.75$.

The values of these nondimensional parameters puts TTP in a case of having quasi-steady lee waves, finite depth, supercritical slope, and nonlinear blocking. This part of parameter space is likely to be common in high-latitude coastal regions. Similar ridges have been studied with nonhydrostatic models (Nakamura et al. 2000; Legg and Huijts 2006) and by observations of two-layer, hydraulically controlled ridges (Armi 1986; Farmer and Armi 1999). Because of the nonlinearity of this ridge case, no theories have been developed that can predict the wave drag that should be seen at TTP. Comparisons can be made to steady theory (Gill 1982; Baines 1995), oscillatory theory for subcritical slopes in infinite depths (Bell 1975a,b), theories with adjustments for finite depth (Khatiwala 2003), theories with adjustments for steep topography (Balmforth et al. 2002; Llewellyn Smith and Young 2003; St. Laurent et al. 2003; Pétrélis et al. 2006), and theories for steady flow over corrugated slopes and isolated ridges on a slope (Thorpe 1992, 1996; MacCready and Pawlak 2001). The simplest wave drag parameterization is for steady flow over an isolated "Witch of Agnesi" ridge with small $Nh_0/U_0$ in infinite depth fluid (Baines 1995, p. 245):

$$D_{\text{wave}} = \frac{\pi}{8}\rho_0 N h_0^2 u_0. \tag{14}$$

Three more relevant wave drag parameterizations are detailed in St. Laurent et al. [2003, Eqs. (24), (22), and (21), respectively]: oscillatory flow over a Witch of Agnesi ridge in an infinite depth fluid, oscillatory flow over a Witch of Agnesi ridge in a finite depth fluid, and oscillatory flow over a knife-edge in a finite depth fluid.

Using the bluff body drag parameterization (13) and these four wave drag parameterizations, the size of the drag at TTP can be put into perspective (Fig. 15). The bluff body drag (13) with $C_D = 1$ underpredicts $D_{\text{form}}$ and $P_{\text{form}}$ significantly. Of the wave drag parameterizations, the one for the steady, infinite-depth flow over the Witch of Agnesi ridge (14) does the best job. The knife-edge parameterization overpredicts the drag, which is understandable because the topography at TTP is shaped more like a Witch of Agnesi ridge than a knife-edge. The two oscillatory, Witch of Agnesi parameterizations for finite and infinite depth flow give the same result, which is somewhat surprising because it is reasonable to think that depth should be an important factor. However, as St. Laurent et al. (2003) points out, in the limit of $\delta/\varepsilon \ll 1$, the parameterization for a finite depth fluid reduces to that of an infinite depth one. At TTP, $\delta/\varepsilon$ is 0.03 and 0.04 for the ridge and headland transects, respectively. It is also somewhat surprising that the steady parameterization would predict the drag better than the oscillatory one. The parameterization for oscillatory flow over a Witch of Agnesi ridge in infinite depth fluid [St. Laurent et al. 2003, Eq. (24)] is
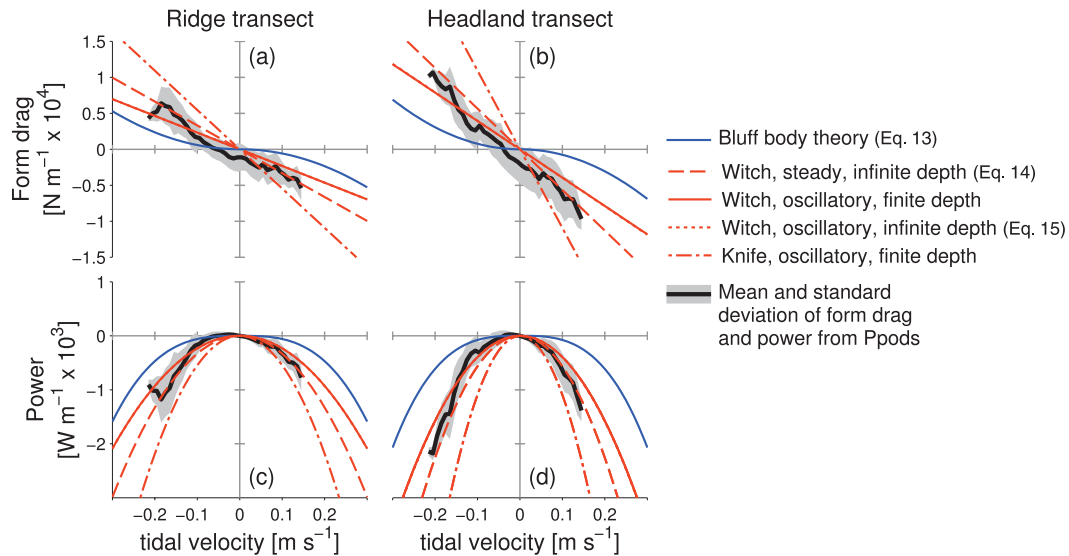
FIG. 15. Four theoretical wave drag parameterizations (red) and the bluff body drag parameterization (blue) are compared to the (a),(b) form drag and (c),(d) power along the ridge transect in (a),(c) and headland transect in (b), (d) transects. Here, the mean (black) and standard deviation (gray) of $D_{form}$ and $P_{form}$ have been calculated over velocity bins of 0.01 m s$^{-1}$. (Note that the parameterizations for oscillatory flow over a "Witch of Agnesi" ridge in finite and infinite depth fluids are nearly equivalent and therefore cannot be seen as separate lines.)

$$D_{\text{unsteady wave}} = \frac{\pi}{8}\rho_0 \frac{[(N^2 - \omega^2)(\omega^2 - f^2)]^{1/2}}{\omega} h_0^2 u_0. \quad (15)$$

In a confined channel, it is a valid assumption to let $f = 0$ s$^{-1}$. Furthermore, $N \gg \omega$ at TTP. In these two limits, the oscillatory drag (15) reduces to the steady drag (14). Finally, (14) requires small $Nh_0/U_0$, which is not true at TTP. We hypothesize that the ridge–headland hybrid topography at TTP makes this parameter less important because in regions where the fluid is blocked, it can travel around the topography rather than over it.

In previous experiments at TTP, the form drag was found to be as much as seven times larger than predicted by bluff body drag with an $O(1)$ drag coefficient (Edwards et al. 2004; McCabe et al. 2006). It was hypothesized that TTP was incredibly efficient at generating drag, possibly because of its shape or the fact that the tidal excursion distance is nearly the same as the topographic length. WM09 suggested that the increased drag was due to the oscillatory nature of the flow creating inertial drag. In this study, we again show that the form drag at TTP is much larger than predicted by bluff body drag. However, now we conclude that it is not due to the inertial drag as hypothesized by WM09 because it was shown to be quite small in section 8. Nor is it due to the tidal excursion distance or shape of TTP. Instead, it is simply that a wave drag law is a more appropriate parameterization than a bluff body drag law since the flow at TTP is stratified and internal waves are generated in addition to eddies.

The underprediction of $D_{form}$ by $D_{BB}$ can also be seen when comparing tidally-averaged power along the two transects (Fig. 16). Here, $P_{BB}$ only accounts for about a third of $P_{form}$. $P_{wave}$ does a much better job; it overestimates tidally averaged $P_{form}$ by only about 25%. This overestimation is due largely to error at low velocities rather than at high velocities when drag is larger.

This experiment was conducted during neap tides. As discussed in section 2, we expect that the form drag would be larger during spring tides owing to faster tidal velocities. To test how much variability there is throughout a spring/neap tidal cycle, $D_{wave}$ and $P_{wave}$ can be calculated using velocities from a tide model of Puget Sound (Lavelle et al. 1988). It is found that tidally-averaged $P_{wave}/L$ over a spring tide is 0.32 W m$^{-2}$, which is 60% larger than tidally-averaged $P_{wave}/L$ during our experiment. This compares well to the average power measured at TTP during a spring tide by Edwards et al. (2004) of 0.72 MW or 0.30 W m$^{-2}$. Averaged over an entire year, $P_{wave}/L = 0.26$ W m$^{-2}$, which is 30% larger than during our experiment.

In addition to comparing $P_{form}$ to theories, it can be compared to our other measurements such as $P_{bulk}$ (section 4b) and $P_{int}$ (section 5) (Fig. 16). Average $P_{bulk}/L$ is 0.19 W m$^{-2}$, which compares well with $P_{form}/L$ along the ridge (0.21 W m$^{-2}$) and headland transects (0.18 W m$^{-2}$). Along the ridge transect, $P_{int}/L$ is about 80% as big as $P_{form}/L$ (Fig. 16). Since the pressure from the Ppods contains internal, external, and nonhydrostatic pressure, we
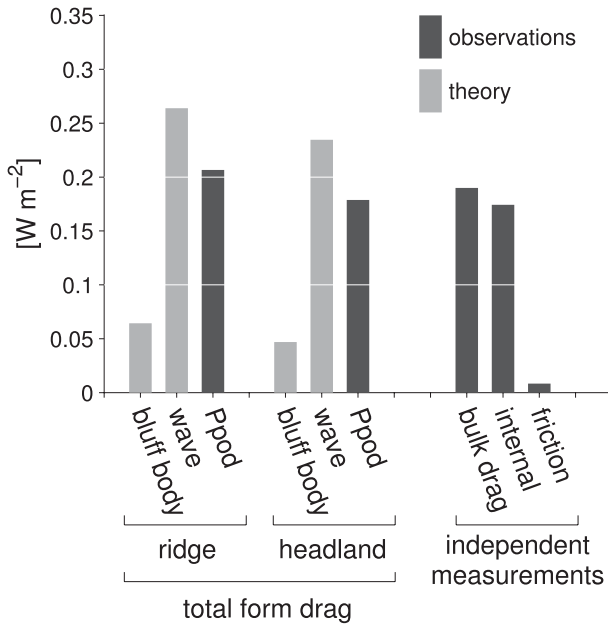
FIG. 16. Time-averaged power that has been calculated in many ways throughout this paper. The two theoretical powers (gray) are from the bluff body drag law (13) and the linear wave drag law (14). The observed $P_{form}/L$ (black) along the ridge and headland transects compare more-closely to the wave drag than to the bluff body drag. $P_{bulk}/L$, $P_{int}/L$ and $P_{friction}/L$ are also shown for comparison.

would expect that $P_{int}$ would be smaller than $P_{form}$. In a numerical model of the region, there is evidence that along the ridge transect $D_{form}$ is mostly made of internal form drag whereas closer to shore, the external form drag begins to play a much larger role (Warner 2012, chapter 4). Finally, the power loss to bottom friction (0.008 W m$^{-2}$) pales in comparison to losses from from drag. This further justifies the fact that models that only use a frictional drag coefficient to parameterize drag in regions of rough topography are going to miss a large part of the drag and energy loss.

## 10. Conclusions

The form drag $D_{form}$ on TTP was measured with bottom pressure sensors. Its magnitude was confirmed by comparing it to drag derived from the shallow water momentum equation ($D_{bulk}$). These methods find similar tidally averaged power losses: $D_{form}/L|_{ridge} = 0.21$ W m$^{-2}$, $D_{form}/L|_{headland} = 0.18$ W m$^{-2}$, and $D_{bulk}/L = 0.19$ W m$^{-2}$. Furthermore, both methods showed that the form drag and power have their biggest magnitude during the strong flood tides becaus of the asymmetry of the strength of the tides (floods are faster than ebbs) and to the asymmetry of the topography (the south side is steeper than the north). Additionally, it was shown that form drag is 30 times larger than frictional drag.

Because of the combination of stratification and topography, a bluff body drag law with an $O(1)$ drag coefficient drastically underestimates the measured form drag. A linear wave drag law gives a much better prediction of the form drag and power. Using the linear wave drag law combined with a tide model of the region, an annual average power loss at TTP of 0.26 W m$^{-2}$ is estimated. Maximum tidally averaged power loss of 0.32 W m$^{-2}$ is found during spring tides, which compares well to the estimate by Edwards et al. (2004). It was also shown that the inertial drag was much smaller than the total form drag, which is different from what was predicted by WM09 for headlands with vertical sidewalls.

Physical mechanisms associated with form drag generation were observed as follows: eddies were seen in the velocity data, internal waves in the potential density data, and elevated levels of turbulent kinetic energy dissipation rates in the microstructure data. Here, $P_{int}$ was 80% as big as $P_{form}$. Maximum values of the spatially averaged dissipation were 25%–50% as big as $P_{form}$ during strong flood tides, which means that while some tidal energy is dissipated locally, it appears that over half of it is carried away from the topography by internal waves and eddies to be dissipated elsewhere.

Overall, even though TTP only accounts for a very small percentage of the energy dissipation in Puget Sound or the world's oceans, the form drag power losses at TTP are 30 times larger than frictional losses over a equivalent flat area. Therefore, it is important that form drag—not just frictional drag—is taken into consideration in larger-scale numerical models. Furthermore, form drag causes energy dissipation throughout the water column, not just in the bottom boundary layer. So simply increasing the bottom friction in numerical models to account for topographic form drag may not lead to momentum and energy losses in the correct locations.
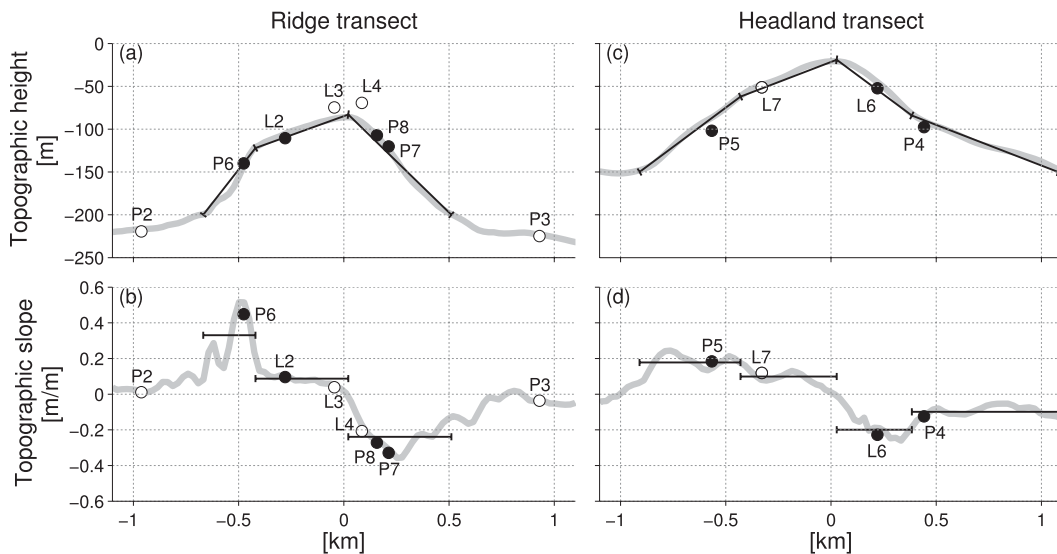
FIG. A1. The locations of the Ppods along the topography on the (a) ridge and (c) headland transects, and (b),(d) the corresponding topographic slopes. The segments that were used to calculate form drag (thin black lines) were chosen to match the topographic height and slope (thick gray lines) as best as possible. Black dots indicate Ppods that were used in the piecewise form drag calculation.

## APPENDIX

## Error Analysis

### a. Ppod pressure errors

In section 3, it was explained how $p'_{bot}$ is calculated from the total Ppod pressure. There are a few sources of error involved in this calculation that need to be elaborated upon.

First, it is possible that removing the sinking events (section 3) resulted in errors because aligning the pressure anomalies before and after each sinking event was done visually. However, these would not be larger than 10% of the range of $p'_{bot}$, and therefore not likely to affect the form drag integral substantially.

A second source of error is due to drifting clocks. This is what rendered the pressure from Lander 7 unusable. It is essential that the clocks are all aligned and keep accurate time because even small differences in timing can result in falsely large pressure anomalies when the background tidal height is subtracted. As an example, if the clock on a Ppod is off by 20 s, due simply to the rate of change of $\rho_0 g \overline{\eta}$, $p'_{bot}$ can be incorrect by 50 Pa. This is the same order of magnitude as the pressure anomalies that create form drag and therefore a very serious problem. All of the other Ppods had newer software than L7 and therefore were not prone to this problem. However, it is something that one must be very careful about when measuring form drag in locations where tidal height changes rapidly.

The mean and 95% confidence interval of $p'_{bot}$ from each Ppod at different points in the tidal cycle was shown in Fig. 6. There is a fair amount of variability from one tidal cycle to the next, which is due in part to natural variability of the maximum tidal velocity during each flood and ebb. However, there is still a statistically significant along-channel pressure slope during the strong floods and ebbs, which shows that, despite this variability, the pressure signals are robust enough to trust our form drag calculations.

### b. Three form drag integration methods

Since Ppods were only located at a few distinct locations along the two transects, multiple ways of calculating form drag with (1) were attempted to see how much sensitivity there is to integration method.

The first method was the simplest: one Ppod from each side of the topography was used. On the ridge transect, the Ppods used were L2 on the north and P8 on the south. The slope was estimated as a constant value of $s = 0.23$, which was taken as positive on the north and negative on the south. A constant $x$ distance was of $l = 500$ m was also used for each side. Essentially this method assumes that TTP is shaped like an isosceles triangle with a bottom length of 1000 m and height of 115 m. The form drag was integrated as

$$D_{\text{form(average)}} = -[p_{L2}sl + p_{P8}(-s)l]. \qquad (A1)$$
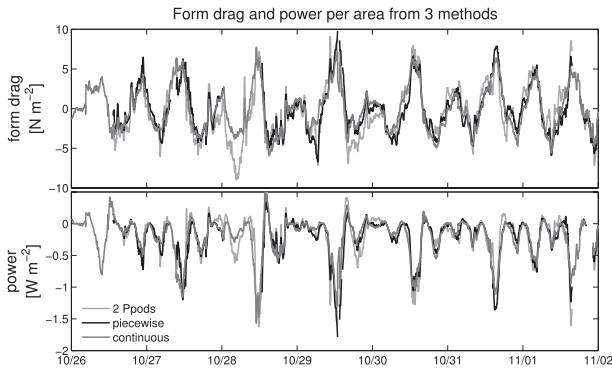
Form drag and power per area from 3 methods



FIG. A2. $D_{form}/L$ and $P_{form}/L$ calculated using three different methods of integration of bottom pressure and slope across the topography. The 2 Ppods method takes the pressure and slope from each side of the topography. The piecewise method breaks the topography into discrete sections each containing one Ppod. The continuous method linearly interpolates the pressure along the transect before integrating.

Along the headland transect, the Ppod on the north was P5 and on the south was L6. The average slope and $x$ distance were 0.165 and 750 m, respectively.

The second method involved piecewise integration across the topography. To do this, discrete sections that traced the shape of the topography were used (Fig. A1). The average slope ($s_1$, $s_2$, etc.) of each section was multiplied by $p'_{bot}$ from the Ppod located within each section and then summed along the length of the transect ($l_1$, $l_2$, etc.). Along the ridge transect, three sections were used and along the headland transect, four sections were used (Fig. A1). It is essential that the form drag integral start and end at the same depth (MacCready et al. 2003). The end depth was chosen to be 200 m on the ridge transect and 150 m on the headland transect. For this method, the form drag along the ridge transect was integrated as

$$D_{form(piecewise)} = -[p'_{P6}s_1l_1 + p'_{L2}s_2l_2 \\ + 0.5(p'_{P8} + p'_{L7})s_3l_3]. \quad (A2)$$

There were three caveats to this method. First, along the ridge transect, the average pressure from P7 and P8 was used in a single section because they were located so close to each other. Second, along the headland transect, L7 failed, so P5 was used instead. Third, the pressures from P2, L3, L4, and P3 were not used because they were located in regions with near-zero topographic slope.

The third method for calculating form drag involved a more continuous integration along the transects. The ridge was broken into 80 points spaced about 25 m apart. The pressure was linearly interpolated from the two Ppods closest to every point:

$$p_{interp} = p_{up}\frac{l_{down}}{l_{up} + l_{down}} + p_{down}\frac{l_{up}}{l_{up} + l_{down}}. \quad (A3)$$

Here, $p_{up}$ and $p_{down}$ are $p'_{bot}$ at the upstream and downstream Ppods located closest to a given point and $l_{up}$ and $l_{down}$ are the distances from that point to the upstream and downstream Ppods, respectively. The slope was calculated from the shipboard ADCP bottom-track depth. Once the pressure and slope were calculated at each point along the transect, (1) could be used directly.

Overall, these three methods give very consistent results for form drag and power (Fig. A2). In Fig. A2, the form drag and power have been divided by the transect length because the transect length differs slightly between the three methods. The average power ($P_{form}/L$) for the three methods calculated over the same time period are nearly equal at 0.216, 0.219, and 0.211 W m$^{-2}$ for the 2 Ppod, piecewise, and continuous methods, respectively.

The consistency between the three methods shows that no matter how form drag is integrated, the calculation is robust. It is possible that the location of the Ppods missed some ''hot spots'' of form drag generation, which would lead to an underestimate of form drag. However, beccause of the similarity between the three methods of form drag integration that used either 2, 4, or 8 Ppods, it also shows that most likely there were enough Ppods deployed across the topography to get an accurate estimate of form drag. Throughout the paper, the piecewise method is used.

REFERENCES

Armi, L., 1986: The hydraulics of two flowing layers with different densities. *J. Fluid Mech.,* **163,** 27–58.

Baines, P. G., 1995: *Topographic Effects in Stratified Flows.* Cambridge University Press, 500 pp.

Balmforth, N. J., G. R. Ierley, and W. R. Young, 2002: Tidal conversion by subcritical topography. *J. Phys. Oceanogr.,* **32,** 2900–2914.

Bell, T. H., 1975a: Lee waves in stratified flows with simple harmonic time dependence. *J. Fluid Mech.,* **67,** 705–722.

——, 1975b: Topographically generated internal waves in the open ocean. *J. Geophys. Res.,* **80,** 320–327.

Bougeault, P., and Coauthors, 1993: The atmospheric momentum budget over a major mountain range: First results of the Pyrex field program. *Ann. Geophys.,* **11,** 395–418.

Bretschneider, D. E., G. A. Cannon, J. R. Holbrook, and D. J. Pashinski, 1985: Variability of subtidal current structure in a fjord estuary: Puget Sound, Washington. *J. Geophys. Res.,* **90** (C6), 11 949–11 958.

Canals, M., G. Pawlak, and P. MacCready, 2009: Tilted baroclinic tidal vortices. *J. Phys. Oceanogr.,* **39,** 333–350.

Dean, R. G., and R. A. Dalrymple, 1984: *Water Wave Mechanics for Engineers and Scientists.* Prentice-Hall, Inc., 353 pp.

Edwards, K. A., P. MacCready, J. N. Moum, G. Pawlak, J. Klymak, and A. Perlin, 2004: Form drag and mixing due to tidal flow past a sharp point. *J. Phys. Oceanogr.,* **34,** 1297–1312.

Emery, W. J., and R. E. Thomson, 2004: *Data Analysis Methods in Physical Oceanography*. 2nd ed., Elsevier Inc, 634 pp.

Farmer, D., and L. Armi, 1999: The generation and trapping of solitary waves over topography. *Science,* **283,** 188–190.

Fox, R. W., and A. T. McDonald, 1998: *Introduction to Fluid Mechanics*. 5th ed., John Wiley & Sons, Inc., 512 pp.

Garrett, C., and E. Kunze, 2007: Internal tide generation in the deep ocean. *Annu. Rev. Fluid Mech.,* **39,** 57–87.

Gill, A. E., 1982: *Atmosphere–Ocean Dynamics*. Academic Press, 662 pp.

Inall, M., T. Rippeth, C. Griffiths, and P. Wiles, 2005: Evolution and distribution of TKE production and dissipation within stratified flow over topography. *Geophys. Res. Lett.,* **32** L08607, doi:10.1029/2004GL022289.

Jayne, S. R., and L. C. St. Laurent, 2001: Parameterizing tidal dissipation over rough topography. *Geophys. Res. Lett.,* **28,** 811–814.

Kelly, S. M., J. D. Nash, and E. Kunze, 2010: Internal-tide energy over topography. *J. Geophys. Res.,* **115,** C06014, doi:10.1029/2009JC005618.

Khatiwala, S., 2003: Generation of internal tides in an ocean of finite depth: Analytical and numerical calculations. *Deep-Sea Res. I,* **50,** 3–21.

Kim, Y.-J., S. D. Eckermann, and H.-Y. Chun, 2003: An overview of the past, present and future of gravity-wave drag parameterization for numerical climate and weather prediction models: Survey article. *Atmos.–Ocean,* **41,** 65–98.

Klymak, J. M., and M. C. Gregg, 2004: Tidally generated turbulence over the knight inlet sill. *J. Phys. Oceanogr.,* **34,** 1135–1151.

Lavelle, J. W., H. O. Mofjeld, E. Lempriere-Doggett, G. A. Cannon, D. J. Pashinski, E. D. Cokelet, L. Lytle, and S. Gill, 1988: A multiply-connected channel model of tides and tidal currents in Puget Sound, Washington and a comparison with updated observations. NOAA Pacific Marine Environmental Laboratory Tech. Rep. ERL PMEL-84, 103 pp.

Legg, S., and K. M. H. Huijts, 2006: Preliminary simulations of internal waves and mixing generated by finite amplitude tidal flow over isolated topography. *Deep-Sea Res. II,* **53,** 140–156.

Llewellyn Smith, S. G., and W. R. Young, 2003: Tidal conversion at a very steep ridge. *J. Fluid Mech.,* **495,** 175–191.

Lott, F., and M. J. Miller, 1997: A new subgrid-scale orographic drag parameterization: Its formulation and testing. *Quart. J. Roy. Meteor. Soc.,* **123,** 101–127.

MacCready, P., and G. Pawlak, 2001: Stratified flow along a rough slope: Separation drag and wave drag. *J. Phys. Oceanogr.,* **31,** 2824–2839.

——, ——, K. A. Edwards, and R. McCabe, 2003: Form drag on ocean flows. *Near-Boundary Processes and Their Parameterization: Proc. 13th 'Aha Huliko'a Hawaiian Winter Workshop,* Honolulu, HI, University of Hawaii at Manoa, 119–130.

McCabe, R., P. MacCready, and G. Pawlak, 2006: Form drag due to flow separation at a headland. *J. Phys. Oceanogr.,* **36,** 2136–2152.

Moum, J. N., and J. D. Nash, 2000: Topographically induced drag and mixing at a small bank on the continental shelf. *J. Phys. Oceanogr.,* **30,** 2049–2054.

——, and W. D. Smyth, 2006: The pressure disturbance of a nonlinear internal wave train. *J. Fluid Mech.,* **558,** 153–177, doi:10.1017/S0022112006000036.

——, and J. D. Nash, 2008: Seafloor pressure measurements of nonlinear internal waves. *J. Phys. Oceanogr.,* **38,** 481–491.

——, M. C. Gregg, R. C. Lien, and M. E. Carr, 1995: Comparison of turbulence kinetic energy dissipation rate estimates from two ocean microstructure profilers. *J. Atmos. Oceanic Technol.,* **12,** 346–366.

Nakamura, T., T. Awaji, T. Hatayama, K. Akitomo, and T. Takizawa, 2000: The generation of large-amplitude unsteady lee waves by subinertial K1 tidal flow: A possible vertical mixing mechanism in the Kuril Straits. *J. Phys. Oceanogr.,* **30,** 1601–1621.

Nash, J. D., and J. N. Moum, 2001: Internal hydraulic flows on the continental shelf: High drag states over a small bank. *J. Geophys. Res.,* **106** (C3), 4592–4612.

Nikurashin, M., and R. Ferrari, 2011: Global energy conversion rate from geostropic flows into internal lee waves in the deep ocean. *Geophys. Res. Lett.,* **38,** L08610, doi:10.1029/2011GL046576.

Officer, C. B., 1976: *Physical Oceanography of Estuaries (and Associated Coastal Waters)*. John Wiley & Sons, Inc., 465 pp.

Oke, P. R., J. S. Allen, R. N. Miller, G. D. Egbert, and P. M. Kosro, 2002: Assimilation of surface velocity data into a primitive equation coastal ocean model. *J. Geophys. Res.,* **107** (C9), 3122–3147.

Pawlak, G., P. MacCready, K. A. Edwards, and R. McCabe, 2003: Observations on the evolution of tidal vorticiy at a stratified deep water headland. *Geophys. Res. Lett.,* **30,** 2234.

Pétrélis, F., S. G. Llewellyn Smith, and W. R. Young, 2006: Tidal conversion at a submarine ridge. *J. Phys. Oceanogr.,* **36,** 1053–1071.

Polzin, K. L., J. M. Toole, J. R. Ledwell, and R. W. Schmitt, 1997: Spatial variability of turbulent mixing in the abyssal ocean. *Science,* **276,** 93–96.

Rudnick, D. L., and Coauthors, 2003: From tides to mixing along the Hawaiian Ridge. *Science,* **301,** 355–357.

St. Laurent, L., S. Stringer, C. Garrett, and D. Perrault-Joncas, 2003: The generation of internal tides at abrupt topography. *Deep-Sea Res. I,* **50,** 987–1003.

Stöber, U., and J. N. Moum, 2011: On the potential for automated realtime detection of nonlinear internal waves from seafloor pressure measurements. *Appl. Ocean Res.,* **33,** 275–285.

Thorpe, S. A., 1992: The generation of internal waves by flow over the rough topography of a continental slope. *Proc. Roy. Soc. Math. Sci.,* **439,** 115–130.

——, 1996: The cross-slope transport of momentum by internal waves generated by alongshore currents over topography. *J. Phys. Oceanogr.,* **26,** 191–204.

Vallis, G. K., 2006: *Atmospheric and Oceanic Fluid Dynamics*. Cambridge University Press, 745 pp.

Warner, S. J., 2012: Using bottom pressure to quantify tidal form drag on a sloping headland. Ph.D. thesis, University of Washington, 131 pp.

——, and P. MacCready, 2009: Dissecting the pressure field in tidal flow past a headland: When is form drag "real"? *J. Phys. Oceanogr.,* **39,** 2971–2984.

Wood, N., A. R. Brown, and F. E. Hewer, 2001: Parameterizing the effects of orography on the boundary layer: An alternative to effective roughness lengths. *Quart. J. Roy. Meteor. Soc.,* **127,** 759–777.